TÉCNICO LISBOA

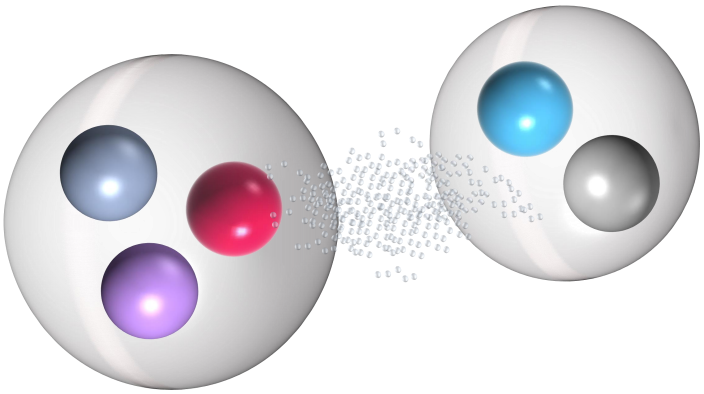

Pentaquarks in QCD

Madalena Carvalho Lourenço

Thesis to obtain the Master of Science Degree in

Engineering Physics

Supervisors: Prof. Gernot Eichmann
Prof. Alfred Stadler

Examination Committee

Chairperson: Prof. Ilídio Pereira Lopes
Supervisor: Prof. Gernot Eichmann
Member of the Committee: Prof. Orlando Olavo Aragão Aleixo e Neves de Oliveira

December 2020

Valeu a pena? Tudo vale a pena
Se a alma não é pequena
Quem quer passar além do Bojador
Tem que passar além da dor
Deus ao mar o perigo e o abismo deu,
Mas nele é que espelhou o céu.

Fernando Pessoa

Acknowledgments

First of all, I would like to express my sincere gratitude and appreciation towards my supervisors, Dr. Gernot Eichmann and Prof. Alfred Stadler, for their infinite patience and unconditional support during these last months, mainly for all the knowledge shared with me. Also, I thank them for correcting my code bugs three hundred times. A special thanks to Prof. Teresa Peña for trusting me towards achieving this thesis project and the encouraging phone calls during this time.

I would also like to thank Prof. Maria José Gomes for guiding me through my whole academic journey, helping me with every decision, and never doubting my capacities. I also thank her for the three-hour phone calls, personal advice, and sometimes cracking the whip on me. I owe a lot to the professor, and I am so grateful for our relationship.

I wish to express my gratitude to Dr. Vanda Lopes for giving me her hand two years ago in a difficult moment and never let me down.

I also want to thank my FCUL and IST colleagues. Namely, Cristiana Ernesto for being my “sister” and accompanied me in every adventure, for supporting me, believing in me, and always have an encouraging word to say. Also, to our funny plane, car, bicycle, cable car, and boat trips during the last years. To my Bia, Beatriz Pereira, for being my partner in this master adventure, for all the five hundred Skype calls during this stage, and I’m so grateful for she has appeared in my life in such a difficult time. Thank you, my girls!

A word of appreciation goes to all my colleagues and professors that were part of my school path from JI Vila de Rei to Liceu Camões.

A special word of appreciation to Matilde for being the most annoying sister in the universe, for watching my presentations during the last 20 years, and demonstrating pride in her older sister every time. I also thank her for always make me laugh. Thank you, my Tidi!

Finally, I want to express my profound gratitude to my parents, for their unconditional support of my choices and for being the first ones to believe that I could do everything, excepting, of course, to see the time on the watch hands and rope skipping. To my mummy, I thank her for all the lessons, and for all the times she said: ”You can do this”. To my dad, for being my first teacher and supporting all my out of the box decisions. Thank you from the bottom of my heart.

Resumo

Durante décadas após a invenção do modelo de quarks por Murray Gell-Mann e, independentemente, por George Zweig em 1964, não havia qualquer evidência que os hadrões fossem formados por outras combinações de quarks e antiquarks para além das mais simples: os mesões são formados por um par quark-antiquark e os bariões por três quarks. No entanto, nas últimas décadas, com o aumento exponencial da quantidade de dados provenientes dos aceleradores de partículas, foram detetados estados que não se enquadram nesta imagem: hadrões exóticos. Estes podem ser explicados se os "novos" mesões forem constituídos por dois quarks e dois antiquarks (tetraquarks) e os bariões por quatro quarks e um antiquark (pentaquarks). As explicações teóricas para estes estados do pentaquark tomam dois rumos distintos: partículas fortemente ligadas, tal como no caso dos hadrões ditos normais, mas com mais constituintes, ou "moléculas" fracamente ligadas semelhantes ao deuterão, mas formados por um mesão e um barião.

O objetivo deste projeto de tese é calcular os estados do pentaquark em QCD no formalismo de Bethe-Salpeter e fazer previsões para os estados observados no LHCb, compostos por quarks leves e charm. A finalidade principal é resolver, numericamente, uma equação a dois corpos para um sistema mesão-barião que acopla os canais principais na equação. No nosso modelo, a interação entre o mesão e o barião é modelada pela troca de um bosão. Após resolver a equação, é calculado o espetro de valores próprios, permitindo assim a determinação das massas dos estados ligados.

Palavras-chave: Equações de Bethe-Salpeter, equação de canais acoplados, hadrões exóticos, pentaquarks.

Abstract

For many decades after the invention of the quark model by Murray Gell-Mann and, independently, George Zweig in 1964, there was no evidence that hadrons are formed from anything other than the simplest combinations of quarks and antiquarks: mesons are formed of a quark-antiquark pair and baryons of three quarks. In the last decade, however, in an explosion of data from hadron colliders, many recently observed states do not fit into this picture: exotic hadrons. They can be explained if the new mesons contain two quarks and two antiquarks (tetraquarks), while the baryons contain four quarks plus an antiquark (pentaquarks). The theoretical explanations for these pentaquark states take two divergent tracks: tightly bound objects, just as in the case of normal hadrons, but with more constituents, or loosely bound “molecules” similar to the deuteron, but formed of a meson and a baryon.

The goal of this thesis project is to calculate pentaquark states in QCD within the Bethe-Salpeter formalism and make predictions for these observed LHCb states made of light and charm quarks. The main objective is to solve, numerically, a two-body equation for a meson-baryon system, which couples the relevant channels in the equation. In our approach, the interaction between the meson-baryon molecule is shaped by one-boson exchanges. Having solved the equation, the eigenvalue spectrum is plotted, allowing the determination of the masses of the bound states.

Keywords: Bethe-Salpeter equations, coupled channel equation, exotic hadrons, pentaquarks.

Contents

List of Tables

List of Figures

List of Abbreviations

BSA(s)	Bethe-Salpeter Amplitude(s)
BSE(s)	Bethe-Salpeter Equation(s)
DCSB	Dynamical Chiral Symmetry Breaking
DSE(s)	Dyson-Schwinger Equation(s)
PCAC	Partial Conserved Axial-vector Current
RL	Rainbow-Ladder
QCD	Quantum Chromodynamics

Chapter 1

Introduction

1.1 Overview

About 60 years ago, a large number of previously unknown particles were discovered, including the four Δ resonances, the six hyperons, and the four K mesons. The Δ resonances were observed in pion–nucleon collisions at the Radiation Laboratory in Berkeley [1]. The hyperons and K mesons were discovered in cosmic-ray experiments [2].

Consequently, the central question was: "How to organize this zoo of particles?". Murray Gell-Mann [3] and George Zweig [4] proposed a model that arranged an organization scheme based on the $SU(3)$ group. The observed hadrons are members of specific representations of $SU(3)$, like the baryons form octets and decuplets, and the mesons form octets and singlets. The hadrons in the same representation have similar masses, and the mass differences are linked to the flavor quantum numbers, the hypercharge Y and the isospin I_z. This model, called the "quark model" states that hadrons are formed by the elementary particles of the $SU(3)$ group, called quarks. The quarks are the prototype particles from which all baryons and mesons are built. The simplest combinations are mesons formed by a quark-antiquark pair ($q\overline{q}$) and baryons by three quarks (qqq). The concept of quarks has become widely accepted in past decades, particularly after discovering new particles whose properties could be successfully interpreted within the quark model framework [5].

However, in recent years, with an explosion of data from hadron colliders, particle physicists have seen a remarkable boost in the knowledge of baryons and mesons in the heavier sector [6–11], and some of these recently observed states do not fit into the quark model picture for hadrons, leading to categorize them as exotics due to their divergent characteristics from the ordinary states. It can be assumed that lower-mass exotic mesons are constituted of four (anti-)quarks, called tetraquarks, and baryons of five (anti-)quarks named pentaquarks. Mainly, exotics are found in the charmonium regions ($c\overline{c}$), motivating the new configurations depicted in Figure 1.1. Recently, a new exotic particle was discovered, suggesting a $cc\overline{cc}$ composition [12].

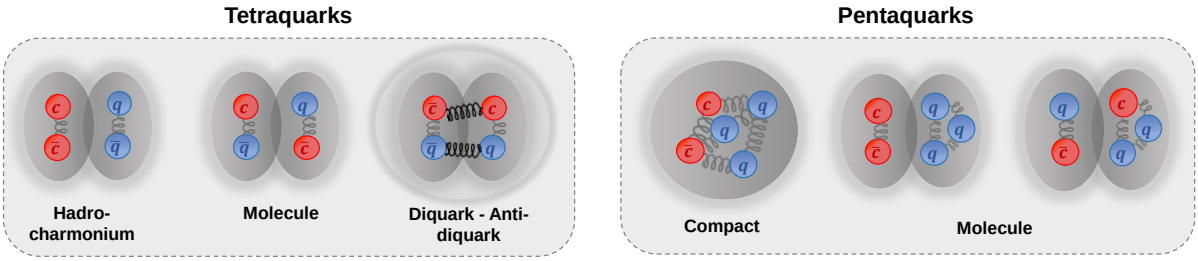

Figure 1.1: Schematic representation of possible tetraquark (*left*) and pentaquark (*right*) configurations. The hadro-charmonia and molecules can be thought of as being bound by hadronic exchanges, while the diquark-anti-diquark and compact pentaquark configurations are connected by colored particle exchanges.

Several theoretical models for exotic states have been developed and take divergent assumptions: tightly bound particles with four or five constituents or loosely bound "molecules" like the deuteron but made of hadrons ([13] and references therein). The binding energy of such molecules is small, so this mass would lie just below the sum of the masses of their constituents. For example, the particle $X(3872)$ discovered in 2003 [14] is a tetraquark state near the $D\overline{D}^*$ threshold, so this is strong evidence that this state is a hadronic molecule formed by the mesons D and $\overline{D}^*$ [15]. The fact that exotic baryons also appear close to thresholds motivates a molecular picture for pentaquark states as well.

Progress in this field also ties into precision measurements of the fundamental properties of hadrons, for instance, the pion, proton, neutron, and simple nuclei to compare with the theoretical calculations and allow for a quantitative description of their internal structure.

1.2 From the quark model to QCD

In the first half of the last century, protons and neutrons were considered as point-like fermions in the Dirac theory with a magnetic moment given by $\mu_D = e/2M$. In 1933 [16], the proton's magnetic moment was determined to be $\mu = (1 + 1.79)\,\mu_D$, meaning that it is not a point-like particle. In 1968, this hypothesis was confirmed in deep inelastic scattering experiments at the Stanford Linear Accelerator Center (SLAC), which showed that protons contained much smaller, point-like objects [17]. This was also a confirmation of the quark model since these objects would later be identified as up and down quarks.

These elementary particles that form hadrons are fractionally charged fermions, and they have baryonic number $B = 1/3$. Initially, they had been assigned three flavors: u (up), d (down) and s (strange) – the light flavors. The most efficient way of adding these quarks to form a hadron is $q\overline{q}$ and qqq, respectively, for mesons with $B = 0$ and baryons with $B = 1$. However, both Gell-Mann and Zweig opened up the possibility of other quark combinations that give rise to the same baryonic numbers. For instance, in 1959, Dalitz and Tuan [18] predicted a resonant structure in $\pi\Sigma$ scattering near the Kp threshold, later called $\Lambda(1405)$, and it was discovered in the 60's through Kp and πp photoproduction [19, 20]. Since then, there has been a longstanding discussion on the structure of this state; its quantum numbers can

be described by uds but not its position in the spectrum because its mass is much lower than expected. This result shows that not all states can be described within a simple quark model framework and points to the existence of exotic states. The $\Lambda(1405)$ could be a KN molecule, carrying a uds quark content complemented by a $u\bar{u}$ or a $d\bar{d}$ pair [21]. Later, the question of multiquark hadrons was raised again, when Lipkin suggested an anticharmed strange baryon, which he named pentaquark [22].

A classification scheme for hadrons was established based upon the notion of (approximate) symmetries of the strong interaction and thus manifest in the appearance of near degenerate multiplets in the hadronic spectrum. This scheme, called the Eightfold way, was proposed by Gell-Mann [23] and Ne'eman [24] in 1961, and it generalized the already successful $SU(2)$ isospin symmetry to flavor $SU(3)_f$, characterized by the hypercharge Y in addition to I_z.

The quark model is an organization scheme that ordered the boost of discovered hadrons in the 1950s and 1960s. However, in its original form, it violates the Pauli exclusion principle. The baryon Ω^- contains three s quarks in relative S-waves with parallel spins (all occupying states with the same quantum numbers). Thus, is there an additional quantum number that allows overcoming this constraint?

In 1965, Han and Nambu [25] considered a model with nine quarks under a $SU(3)_f \times SU(3)_f$ symmetry, and in 1971, Fritzsch and Gell-Mann expanded the idea, considering that the nine quarks were grouped into three triplets of a new quantum number, called color. The color symmetry is an exact symmetry that later was built up as a gauge group where the interaction was given by massless bosons called gluons, which interact with themselves, and this theory is called Quantum Chromodynamics (QCD) [26, 27]. Currently, we know six flavors of quarks: u, d, s (strange), c (charm), b (beauty/bottom), and t (top), and each one can take a color charge red, green, or blue.

Quantum Chromodynamics is the quantum field theory that explains the strongest force in nature - the strong force that keeps quarks and gluons together inside nuclei. Despite all advances, several crucial questions remain open: What enables the formation of the unnaturally light pions in contrast to the ρ-meson? How to explain the origin of more than 98% of the mass of the observable universe? Why are many predicted resonances in the higher mass spectrum? The answer to these questions may be based on two of QCD's emergent phenomena: confinement and Dynamical Chiral Symmetry Breaking (DCSB).

The quarks and gluons are QCD's building blocks. Gluons not only interact with quarks but with themselves, giving the theory its non-Abelian character. The gluon self-interaction leads to the reduction of the coupling constant α_s with increasing energy [28, 29], called asymptotic freedom, allowing the use of perturbation theory to solve QCD at high energies. However, at large distances of the order of the hadron's size, $\alpha_s \sim O(1)$ and perturbation theory no longer works. Moreover, isolated colored particles like quarks and gluons have never been seen, and no matter how hard a hadron is struck, it never breaks apart, due to confinement. Another characteristic feature of QCD is the dynamically generated enhancement of the light quark masses at small momenta, which are several hundred MeV larger than their current quark masses. This is called dynamical chiral symmetry breaking, and implies that the mass remains non-zero even when the current quark mass is zero. Consequently, if there is DCSB, there are massless Goldstone bosons, which can be identified with the light pseudoscalar mesons [30].

A detailed understanding of how gluons and quarks interact inside hadrons, and how to determine their internal structure, remains a challenge in hadron physics. The new observations in the heavy sector may shed light on the study of these features, as well as on the origin of mass in the visible universe, the lightness of the pion, and the interaction mechanisms seen at work for baryons that lead to exotic hadrons and, in particular, multiquark states.

1.3 Experimental observations of pentaquarks

After 50 years without robust experimental candidates for pentaquarks, in 2015 a short-lived pentaquark was observed through the decay of unstable particles in the LHCb experiment at CERN [9]. This new pentaquark is not the one known as Θ^+, which had been seen back in 2003 and was later pronounced a "mirage"; it is almost three times heavier and contains different kinds of quarks, namely $c\bar{c}$.

Studying the decays of $\Lambda_b^0 \to J/\psi K^- p$, particularly the spectrum of the $J/\psi p$ decay mode mass, the LHCb collaboration established the existence of two pentaquark states constituted by $c\bar{c}uud$, making them "charmonium" pentaquarks.

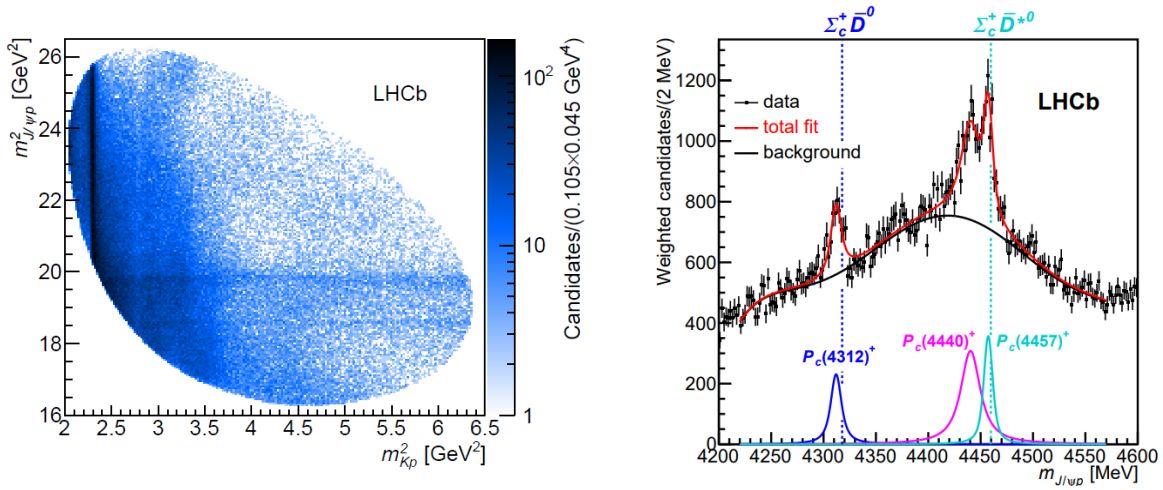

Figure 1.2: *Left*: Dalitz plot of $\Lambda_b^0 \to J/\psi K^- p$ candidates. The vertical bands correspond to the Λ^* resonances. The horizontal bands correspond to the $P_c(4312)^+$, $P_c(4440)^+$ and $P_c(4457)^+$ structures at $m^2_{J/\psi p} = 18.6$, 19.7 and 19.9 GeV^2, respectively. *Right*: Fit to the weighted $m_{J/\psi p}$ distribution, which is used to determine the central values of the masses and widths of the P_c^+ states. The mass thresholds for the $\Sigma_c^+\overline{D}^0$ and $\Sigma_c^+\overline{D}^{*0}$ final states are superimposed [11].

In 2019, combining the data from Run 1 and Run 2 and having a better resolution near the peaks, [11], the LHCb collaboration discovered a third pentaquark, labeled as $P_c(4312)^+$, which was observed with a statistical significance of 7.3σ. There is also 5.4σ evidence that the mass peak in the Run 1 data associated with $P_c(4450)^+$ actually consists of two peaks, which suggests that these correspond to two different pentaquarks, $P_c(4440)^+$ and $P_c(4457)^+$. In these fits, $P_c(4380)^+$ can neither be confirmed nor contradicted. The results are represented in the Figure 1.2. The three peaks are narrow, which means that the pentaquark particles have relatively long lifetimes before they decay, suggesting that

these states resemble molecules holding a baryon and a meson bound together by a residual strong force, as represented by the molecules in Figure 1.1.

The masses of the $P_c(4312)^+$ and $P_c(4457)^+$ lie very close to the threshold energies of $\Sigma_c^+\overline{D}^0$ and $\Sigma_c^+\overline{D}^{*0}$ ($[duc]\,[u\bar{c}]$), namely by 5 MeV and 2 MeV, respectively. The $P_c(4440)^+$ could be another $\Sigma_c^+\overline{D}^*$ state, with about 20 MeV of binding energy. This adjacency to the thresholds provides strong evidence to a meson-baryon molecule explanation. Even though $\Sigma_c\overline{D}$ combinations are the most plausible candidates, other possibilities that can produce these states have been studied such as $J/\psi p$, $\eta_c p$, and $\Lambda_c D$.

Since there is no definitive explanation, several groups carried out detailed analyses in order to identify the pentaquarks' internal structure along different tracks, such as hadronic molecules [15, 31–36], diquark-triquark [37–39], or diquark-diquark-antiquark [40, 41] explanations.

The complete story of exotic states is far from the end, and more experimental data will enrich our knowledge in subsequent years. There have been some proposals to look for them in other processes like $\Lambda_b \to \chi_{c1} p K^-$ [42], photoproduction [43], heavy-ion collisions [44], and pion-nucleon reactions [37]. These new data will provide a thorough test of competing theoretical ideas.

1.4 The goal of the thesis

The goal of this thesis is to calculate pentaquark states in QCD within the Bethe-Salpeter formalism and investigate the spectrum and structure of the observed LHCb pentaquark states. The main objective is to numerically solve a two-body equation for a meson-baryon system, which couples the relevant channels in the equation through boson exchanges.

In Chapter 2 we recapitulate some basic QCD concepts, such as its action, flavor symmetries, fundamental features, and the bound-state formalism from Green functions to Dyson-Schwinger and Bethe-Salpeter equations. In Chapter 3, we describe our coupled equations, including the suitable channels to form the proper pentaquark content and the exchanged particles. A set of numerical techniques to solve the BSE, comparisons with other models, and some features of these systems are presented in Chapter 4. The procedure to determine the coupling constants of the systems is presented in the Chapter 5. Our results are given in Chapter 6. We present our conclusions and further work in 7 as well as our conclusions. In Appendix A, useful mathematical details on the BSE calculations are further explained, and in Appendix B the relevant properties of the particles considered in the thesis are given.

Chapter 2

From QCD action to bound state equations

A quantum field theory is characterized by its action or, equivalently by its Lagrangian. In classical mechanics, the information about the movement of a particle is given via the Euler-Lagrange equations, while in quantum field theory, the Dyson-Schwinger equations of motion relate the Green functions to each other, and the latter encode all properties of the theory.

This chapter outlines some basic concepts of QCD, from the QCD action to dynamical chiral symmetry breaking. Also, we introduce the theoretical framework of Bethe-Salpeter and Dyson-Schwinger equations and their applications to hadron physics. Many studies have been performed in the Bethe-Salpeter approach providing a solid background for this work. We work in the Euclidean metric.

2.1 QCD concepts

Quantum Chromodynamics is a quantum field theory that describes quarks and gluons through its Lagrangian or action. At large energies/small distances (usually called ultraviolet or UV region), the interaction between quarks and gluons is weak and can be described by perturbative methods, while at low energies/long distances (infrared or IR region), the QCD coupling constant becomes strong and perturbative methods are no large suitable to describe the interaction.

2.1.1 QCD action

The QCD action is renormalizable, Poincaré invariant, and locally color gauge invariant under $SU(3)_c$. Based upon these principles, it is described in terms of quark (ψ) and gluon fields (A_μ^a) as

$$S_{QCD} = \int d^4x \left[\overline{\psi} \left(-\not{D} + M \right) \psi + \frac{1}{4} F_{\mu\nu}^a F_{\mu\nu}^a \right], \tag{2.1}$$

where the covariant derivative is $D_\mu = \partial_\mu + igA_\mu$, the gluon field strength tensor is $F_{\mu\nu} = \partial_\mu A_\nu - \partial_\nu A_\mu + ig\left[A_\mu, A_\nu\right]$ and M is the quark mass matrix. The quark fields, ψ and $\overline{\psi}$, actually depend on three

indices, $\psi_{\alpha,i,f}$, where α stands for the Dirac structure since quarks are fermions, i is the color index that accounts for the possible three colors (red, green and blue), and f represents the flavor. The gluon field A^a_μ depends on the generator index a of $SU(3)_c$ and on the Lorentz index μ because it has spin 1.

The symmetries of the theory are implemented by groups. The color and flavor indices portend that the fields transform under $SU(3)_c$ and $SU(N_f)$, respectively. N_f represents the number of flavors considered.

In QCD, there are eight gluon fields, one for each generator $t_a = \lambda_a/2$ of the group $SU(3)_c$, where λ_a are the Gell-Mann matrices. These generators are the basis of the color algebra and obey the commutation relation $[t^a, t^b] = if^{abc}t^c$, where f^{abc} are the structure constants. This allows for the expansion of A_μ into the gluon fields A^a_μ, given by $A_\mu = A^a_\mu\, t^a$, and consequently the gluon field strength tensor $F_{\mu\nu} = F^a_{\mu\nu}t^a$. The additional term in $F_{\mu\nu}$ proportional to $[A_\mu, A_\nu]$ appears due to the non-Abelian character of QCD, which encodes the gluon self-interactions: the three- and four-gluon vertex. The gluon self-interactions are believed to be the origin of two QCD emergent phenomena, namely dynamical chiral symmetry breaking and confinement.

2.1.2 Noether's theorem and currents

The quark part of the Lagrangian depends on flavor through the quark fields. The transformation of the quark fields under $SU(N_f)$ introduces new effects due to flavor symmetries breaking.

To study flavor symmetries, one needs to enunciate Noether's theorem: Any continuous symmetry transformation which leaves the action invariant implies the existence of conserved currents, where the associated charge is a constant of motion. If we consider the following global transformation: $\varphi'(x) = (e^{i\epsilon_a t_a})_{ij}\varphi_j = \varphi_i + \delta\,\varphi_i$, where ϵ_a is a constant parameter, the variation of the action with respect to ϵ_a is given by

$$\begin{aligned}\delta S = \int_V d^4x\,\delta\mathcal{L} = \int_V d^4x \sum_i \left[\frac{\partial\mathcal{L}}{\partial\varphi_i}\delta\varphi_i + \frac{\partial\mathcal{L}}{\partial(\partial_\mu\varphi_i)}\delta(\partial_\mu\varphi_i)\right] \\ = \int_V d^4x \left[\partial_\mu\Bigg(\underbrace{\sum_i \frac{\partial\mathcal{L}}{\partial(\partial_\mu\varphi_i)}\delta\varphi_i}_{-\epsilon_a j^\mu_a}\Bigg) + \sum_i \Bigg(\underbrace{\frac{\partial\mathcal{L}}{\partial(\partial\varphi_i)} - \delta_\mu\frac{\partial\mathcal{L}}{\partial(\partial_\mu\varphi_i)}}_{=0 \text{ for classical solutions}}\Bigg)\delta\varphi_i\,,\end{aligned} \tag{2.2}$$

where j^μ_a represents the current associated to each generator, and the corresponding charges Q_a are written as:

$$\partial_\mu j^\mu_a = -\frac{\delta\mathcal{L}}{\delta\epsilon_a}\,, \qquad Q_a(t) = \int d^3x\, j^0_a(x). \tag{2.3}$$

In the case of the classical action being invariant under the transformation, $\delta S = 0$, and consequently there exists one conserved current along the classical trajectories and a corresponding conserved charge for each generator of the group. If a field does not obey the classical equations of motion or if the symmetry is classically broken, the currents and charges are not conserved, but they are still well-defined.

Flavor symmetries

The properties of the Lagrangian under the global flavor transformations $U(1)_V$, $SU(N_f)_V$, $SU(N_f)_A$ and $U(1)_A$ only affect the quark fields since only they carry flavor indices. Let us consider the following transformations, where ϵ_a is a parameter and t_a are the generators of the group:

$$e^{i\epsilon} \in U(1)_V\,, \qquad e^{i\sum_a \epsilon_a t_a} \in SU(N_f)_V\,, \qquad e^{i\gamma_5\epsilon} \in U(1)_A\,, \qquad e^{i\gamma_5\sum_a \epsilon_a t_a} \in SU(N_f)_A\,. \tag{2.4}$$

The subscripts V and A imply that these transformations will induce vector and axial-vector currents.

- $\mathbf{U(1)_V}$: The Lagrangian is invariant under global phase transformations, $\varphi'(x) = e^{i\epsilon}\varphi(x)$. The vector current, according to the definition in equation (2.2), and its divergence are given by:

  $$V^\mu = \overline{\psi}\gamma^\mu\psi\,, \quad \partial_\mu V^\mu = 0\,. \tag{2.5}$$

  Since the current is conserved, the associated charge $Q_V/3$ is a constant of motion. It corresponds to the baryonic number, which entails the baryonic quantum number conservation.

- $\mathbf{SU(N_f)_V}$: The mass term in the Lagrangian is no longer invariant if quark masses are different; then it is said that the symmetry is explicitly broken. The corresponding vector current and its divergence are

  $$V_a^\mu = \overline{\psi}\gamma^\mu t_a\psi\,, \quad \partial_\mu V_a^\mu = i\,\overline{\psi}[M, t_a]\,\psi\,. \tag{2.6}$$

  The generators t_3 and t_8 are diagonal and commute with the mass matrix M, so the currents V_3^μ and V_8^μ are still conserved, and their associated charges define the third component of isospin (I_z) and the hypercharge (Y), respectively.

- $\mathbf{U(1)_A}$: This symmetry is not conserved after quantization, leading to the so called $U(1)_A$ anomaly. Here,

  $$A^\mu = \overline{\psi}\gamma^\mu\gamma^5\psi\,, \qquad \partial_\mu A^\mu = 2i\,M\,\overline{\psi}\gamma_5\psi + \frac{g^2 N_f}{16\pi^2}\tilde{F}_a^{\mu\nu}F_{\mu\nu}^a \tag{2.7}$$

  are the axial-vector current and the respective divergence, where the dual field strength tensor is $\tilde{F}^{\mu\nu} = \frac{1}{2}\epsilon^{\mu\nu\alpha\beta}F_{\alpha\beta}$. Even in the chiral limit, when $M = 0$, the second term, which is called topological charge density, in the current divergence is non-zero due to regularization.

- $\mathbf{SU(N_f)_A}$: Under the axial-vector transformations, the symmetry is explicitly broken by the mass term, and

  $$A_a^\mu = \overline{\psi}\gamma^\mu\gamma^5 t_a\psi\,, \qquad \partial_\mu A_a^\mu = i\,\overline{\psi}\{M, t_a\}\gamma_5\psi \tag{2.8}$$

  are the axial-vector current and respective divergence.

  When the quark masses are equal, the divergence is given by $\partial_\mu A_a^\mu = 2im\,\overline{\psi}\,t_a\gamma_5\,\psi$, which is called the Partially Conserved Axial-vector Current (PCAC) relation, because in the chiral limit, when the quark masses are equal to zero, the axial-vector current is conserved.

2.1.3 Dynamical chiral symmetry breaking and the mass function of QCD

In nature, quarks have mass; accordingly, chiral symmetry cannot be an exact symmetry of QCD, leading to an explicit chiral symmetry breaking due to the quark mass term. Thus, the would-be Goldstone bosons acquire a non-zero mass, but they are still much lighter than the other hadrons [30]. For instance, the mass of the pion, a Goldstone boson, is around 140 MeV, while the mass of the vector ρ-meson can be estimated by the sum of the "constituent-quark masses" (m_ρ = 770 MeV). This behavior is described by the Gell-Mann-Oakes-Renner (GMOR) relation

$$M_p^2 F_p^2 = -\frac{2 m_0}{N_f} \langle \psi \overline{\psi} \rangle \,, \tag{2.9}$$

where M_p is the mass of the pseudoscalar boson, F_p is the decay constant, m_0 the current-quark mass, and N_f the number of flavors. A non-vanishing vacuum chiral condensate $\langle 0 | \, \overline{\psi} \psi \, | 0 \rangle$ indicates that the system is in the Nambu–Goldstone mode, and allows us to relate the degree of DCSB with physical quantities.

Besides, the quark condensate is the order parameter of DCSB that modifies the structure of the QCD vacuum, and its interaction with quarks equips them with a large dynamical mass that makes the transition between a current quark m_0 to a dynamically generated constituent quark given by the mass function $M(p^2)$, whose behavior is represented in Figure 2.1.

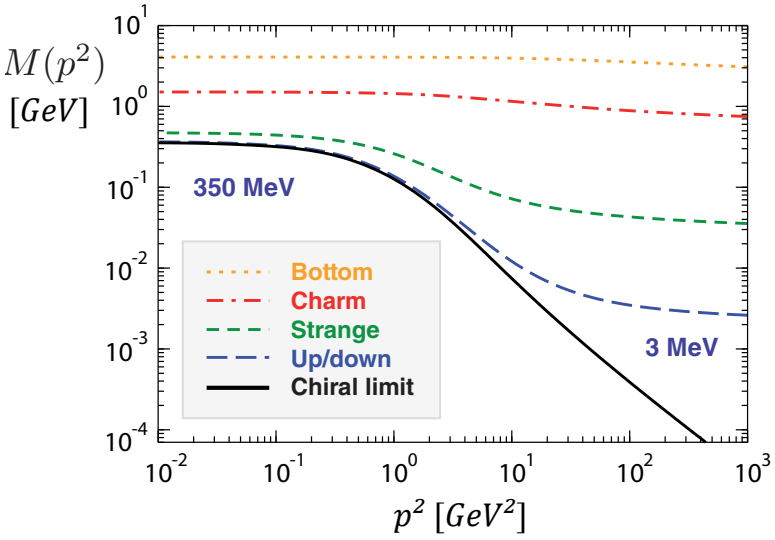

Figure 2.1: The mass function generated non-perturbativly by DCSB. In the small p region, the mass function can ve viewed as a constituent quark mass, while for large p becomes the current-quark mass [45].

2.2 Dyson-Schwinger Equations

The Dyson-Schwinger equations (DSEs) are a non-perturbative and infinite system of coupled equations that relate the correlation functions of a quantum field theory to each other, like the dressed quark and

gluon propagators, and the quark-gluon vertex. In principle, a complete knowledge of all correlation functions would determine the properties of the theory completely [46].

All physical properties can be extracted from the n-point correlation functions, called the Green's functions, which are defined as the vacuum expectation values of the time-ordered product of n fields:

$$G(x_1 \dots x_n) = \langle 0 | \, \mathsf{T} \, \phi(x_1) \dots \phi(x_n) | 0 \rangle = \frac{\int \mathcal{D}\phi \, e^{-S[\phi]} \phi(x_1) \dots \phi(x_n)}{\int \mathcal{D}\phi \, e^{-S[\phi]}} \,, \tag{2.10}$$

where $\phi(x)$ is the classical field, T is the time-ordering operator, and $G(x_1 \dots x_n)$ represents the average over all field configurations with Euclidean probability distribution $e^{-S[\phi]}$.

The full n-point correlation functions can be generated by adding a source term to the partition function and applying functional derivatives. The partition function $Z[J]$ is given by

$$Z[J] = \int \mathcal{D}\phi \; e^{-[S[\phi] - \int d^4x \, \phi(x) J(x)]} \,, \tag{2.11}$$

where $\int d^4x \, \phi(x) J(x)$ is a source term.

Then, one takes functional derivatives of $Z[J]$ with respect to the source $J(x)$:

$$\frac{i\delta}{\delta J(x_1)} \dots \frac{i\delta}{\delta J(x_n)} \, Z[J] = \int \mathcal{D}\phi \, e^{-[S[\phi] + \int d^4x \, \phi(x) J(x)]} \, \phi(x_1) \dots \phi(x_n) \,. \tag{2.12}$$

Comparing the previous result with Eq. (2.10), we deduct the following by setting the source terms to zero:

$$G(x_1 \dots x_n) = \frac{1}{Z[0]} \frac{i\delta}{\delta J(x_1)} \dots \frac{i\delta}{\delta J(x_n)} \bigg|_{J=0} Z[J] \,. \tag{2.13}$$

Besides, not only one can derive the correlation functions from the partition function, but also reconstruct it if the Green functions are known. Thus, these quantities are equivalent to describe a quantum field theory.

In the following, we leave the J dependence until the end so that we can generalize eq. (2.13) to an arbitrary correlation function f as

$$\langle f[\phi(x_1) \dots \phi(x_n)] \rangle_J = \frac{1}{Z[J]} \, f\left[\frac{i\delta}{\delta J(x)}\right] Z[J] \,. \tag{2.14}$$

The DSEs follow from the invariance of the generating functional under the variation $\phi(x) \to \phi(x) + \epsilon(x)$ of the fields, leading to:

$$\left\langle \frac{\delta S[\varphi]}{\delta \varphi(x)} \right\rangle_J = \frac{1}{Z[J]} \frac{\delta S}{\delta \varphi} \left[\frac{i\delta}{\delta J(x)}\right] Z[J] = J(x) \,, \tag{2.15}$$

where in the first equality we made use of eq. (2.14). This is the generating DSE since by taking successive functional derivatives, it generates a tower of DSEs that relates the correlation functions.

We can define a new correlation function, that by performing functional derivatives from the effective action $\Gamma[\varphi]$ generates the one-particle irreducible Green functions. Firstly, one redefines the partition function in terms of the effective action $\Gamma[\varphi]$ written as

$$Z[J] = e^{-(\Gamma[\varphi] - \int d^4x\, \varphi(x) J(x))}\,, \tag{2.16}$$

where $\varphi(x)$ is the vacuum expectation value of the classical field $\phi(x)$ in the presence of a source.

Hence, one can rewrite the DSE-generating equation (2.15) for the one-point irreducible correlation functions as

$$\frac{\delta\Gamma[\varphi]}{\delta\varphi(x)} = \frac{\delta S}{\delta\phi}\left[\varphi(x) + \int_y \left(\frac{\delta\,\Gamma^2[\varphi]}{\delta\varphi(x)\varphi(y)}\right)^{-1} \frac{i\delta}{\delta\varphi(y)}\right], \tag{2.17}$$

where $\frac{\delta S}{\delta\phi}[\varphi(x)]$ contains the classical equations of motion and the remaining terms the quantum "effects", which includes the one-particle irreducible two-point function $\left(\frac{\delta\,\Gamma^2[\varphi]}{\delta\varphi(x)\varphi(y)}\right)^{-1}$, the propagator. Higher derivatives with respect to the gluon and quark fields A^μ, ψ and $\overline{\psi}$ of the left-hand side of equation (2.17) gives the system of DSEs for the n-point Green functions.

For the quark DSE, we perform the derivative of the effective action with respect to the quark and antiquark fields, ψ and $\overline{\psi}$, and a Fourier transformation to obtain the equation in momentum space, which is written as:

$$S^{-1}(p) = Z_2(i\not{p} + m_0) + \Sigma(p)\,, \tag{2.18}$$

where m_0 is the bare quark mass, Z_2 is the renormalization constant and $\Sigma(p)$ is the quark self-energy. In this case, the first term $(i\not{p} + m_0)$ represents the classical equation of motion for the quark and the second term is the quantum contribution, which is the quark self-energy given by

$$\Sigma(p) = -\frac{4}{3} g^2\, Z_{1F} \int_q i\gamma^\mu S(q) D^{\mu\nu}(k) \Gamma^\nu(q,p). \tag{2.19}$$

It includes the gluon propagator $D^{\mu\nu}$, the bare vertex $igZ_{1F}\gamma^\mu$, and the dressed quark-gluon vertex $g\Gamma^\nu$, where g is the coupling constant and Z_{1F} is the renormalization constant.

The solution of the quark DSE is the full quark propagator:

$$S(p) = \frac{Z_f(p^2)}{p^2 + M(p^2)^2}(-i\not{p} + M(p^2))\,, \tag{2.20}$$

where $M(p^2)$ is the quark mass function and $Z_f(p^2)$ the renormalization function. The quark propagator is graphically represented in Figure 2.2.

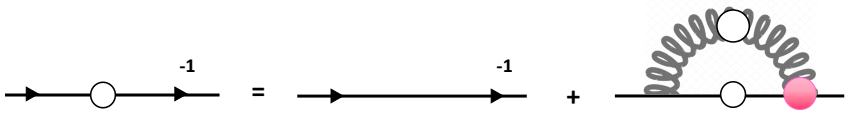

Figure 2.2: Graphical representation of the quark propagator (DSE) given in equation (2.20).

The gluon propagator in Landau gauge is given by

$$D^{\mu\nu}(k) = \frac{Z(k^2)}{k^2}\left(\delta^{\mu\nu} - \frac{k^\mu k^\nu}{k^2}\right), \tag{2.21}$$

where k is the gluon momentum.

The quark-gluon vertex depends on 12 Dirac tensors,

$$\Gamma^{\mu}(k) = \sum_{i=1}^{12} f_i \, \tau_i^{\mu}(k) \,, \tag{2.22}$$

where f_i are the Lorentz invariant dressing functions and τ_i are the Dirac basis elements.

As previously described, the fully dressed propagators and vertices can be determined as solutions of their own DSEs by taking derivatives of the effective action as indicated by equation (2.17). The classical parts are given by the Feynman rules. The Feynman propagators and vertices correspond to the two- and three-point correlation functions at tree-level, respectively.

The most general form of the Green functions follows from the Lorentz invariance, so one can expand the correlation functions in Lorentz-invariant dressing-functions and Lorentz-covariants tensors that inherit the symmetries of G:

$$G^{\mu\nu\ldots}_{\alpha\beta\ldots}(p_1 \ldots p_n) = \sum_{i=1}^{N} f_i \left(p_1^2, p_2^2, p_1 \cdot p_2, \ldots\right) \tau_{i,\alpha\beta\ldots}^{\mu\nu\ldots}(p_1, \ldots p_n) \,, \tag{2.23}$$

where f_i are the Lorentz invariant dressing functions that only depend on invariant quantities, and τ_i are the Lorentz-covariant tensors that depend on all momentum variables.

For example, the quark propagator is deduced from the Lorentz invariance in the following way: the propagator can only depend on two Dirac structures $\{I, \not{p}\}$ since the remaining ones have wrong parity when including the γ_5 matrix. Thus, the most general structure with these tensors is the one given in eq. (2.20).

2.3 Bound state equations

Bound states appear as poles in the n-point Green functions, which encode hadron properties. In particular, a meson corresponds to a pole in the four-point and a baryon in the six-point Green functions, $G^{(2)}$ and $G^{(3)}$, or correspondingly in the scattering matrices, $T^{(2)}$ and $T^{(3)}$. In the Euclidean metric, the total momentum at the pole $P^2 = -M^2$ corresponds to a bound state mass, M, which is determined by solving the corresponding Bethe-Salpeter Equation (BSE) [46, 47].

2.3.1 Dyson's equations

In order to derive the BSE, the starting point is the generalized Dyson equation for the n-point Green functions $G^{(n)}$ or equivalently for the n-point scattering matrix $T^{(n)}$, given by:

$$\begin{aligned} G^{(n)} &= G_0^{(n)} + G_0^{(n)} \, K^{(n)} \, G^{(n)} \,, \\ G^{(n)} = G_0^{(n)} + G_0^{(n)} \, T^{(n)} \, G_0^{(n)} \quad &\Leftrightarrow \quad T^{(n)} = K^{(n)} + K^{(n)} \, G_0^{(n)} \, T^{(n)} \,, \end{aligned} \tag{2.24}$$

where $G_0^{(n)}$ is the product of n disconnected dressed quark propagators, $G^{(n)}$ is the amputated and

connected part of the n-point functions, $K^{(n)}$ corresponds to the n-point scattering kernel, and $T^{(n)}$ is the connected and fully amputated scattering kernel. The last equation in (2.24) is depicted in Figure 2.3 - *left*. Also, its inverse is schematically written as:

$$\left(G^{(n)}\right)^{-1} = \left(G_0^{(n)}\right)^{-1} - K^{(n)}\,, \quad \left(T^{(n)}\right)^{-1} = \left(K^{(n)}\right)^{-1} - G_0^{(n)}\,. \tag{2.25}$$

It establishes a relation between the two-particle irreducible kernel and the Green function $G^{(n)}$ or scattering matrix $T^{(n)}$.

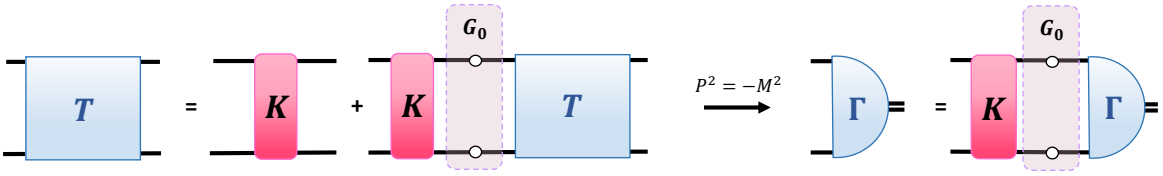

Figure 2.3: The Dyson equation (2.24) for a four-point scattering matrix (*left*). Schematic representation of the bound-state equation for the BS amplitude at the pole position (*right*).

Then, at the pole, the corresponding BS wave function Ψ is the residue of the Green function $G^{(n)}$ and the BS amplitude Γ is the residue of the scattering matrix $T^{(n)}$,

$$G^{(n)} \to \mathcal{N}\frac{\Psi\overline{\Psi}}{P^2 + M^2}\,, \quad T^{(n)} \to \mathcal{N}\frac{\Gamma\overline{\Gamma}}{P^2 + M^2}\,, \quad \Psi = G_0^{(n)}\Gamma\,, \tag{2.26}$$

where P is the total momentum at the pole, and $\mathcal{N}$ is the normalization constant that depends on the spin of the resulting particle. For instance, the propagators of free spin-0 and spin-1/2 particles are, respectively, given by:

$$J = 0: \ \frac{1}{P^2 + M^2} \qquad J = \frac{1}{2}: \ \frac{-i\not{p} + M}{P^2 + M^2} = 2M\frac{\Lambda_+(P)}{P^2 + M^2}, \tag{2.27}$$

which means that the normalization constant $\mathcal{N}$ is 1 in the scalar case and $2M$ in the fermion case. $\Lambda_+(P) = (1 + \hat{\not{P}})/2$ is the positive-energy projector, with $\hat{P}$ being the normalized total momentum $\hat{P} = P/\sqrt{P^2}$.

Inserting equation (2.26) into the Dyson equations (2.24), we identify the pole in G and T by comparing the residues on both sides of the equations that yield the homogeneous equation at the pole, either formulated in terms of the wave function Ψ or the amplitude Γ:

$$\Psi^{(n)} = G_0^{(n)}K^{(n)}\Psi^{(n)}, \quad \Gamma^{(n)} = K^{(n)}G_0^{(n)}\Gamma^{(n)}. \tag{2.28}$$

This is called the Bethe-Salpeter Equation. In order to solve this equation, one needs knowledge of the propagators S_i and the kernel. More details on the procedure to solve BSEs are described in Chapter 4.

For example, the Bethe-Salpeter equation for a quark-antiquark bound state is the particular case of

equation (2.28) for n = 2. If we drop for now the flavor and color indices, the equation is given by:

$$\Gamma^{\mu_j}_{\alpha\beta}(p,P) = \int_q K_{\alpha\gamma,\delta\beta}(p,q,P) \left\{ S(q,P)\, \Gamma(q,P)^{\mu_j}\, S(q,P) \right\}_{\gamma\rho} \tag{2.29}$$

where $S(q,P)$ is the quark propagator from eq. (2.2). This equation is schematically represented in Figure 2.3 - *right*.

Chapter 3

Pentaquarks

A pentaquark system constitutes a five-body problem, which is difficult to solve on technical grounds, considering the large number of independent momenta and tensor structures in the equation. However, the problem can be simplified to a two-body system where the pentaquark is described as a "molecule" made of a baryon and a meson as shown in Figure 3.1. A formal analogy is the reduction of the three-body problem for a baryon to a quark-diquark picture, which also results in a two-body system with fermion (quark) and boson (diquark) constituents [45, 48].

In the case of pentaquarks, the degrees of freedom are mesons and baryons, where the interaction kernel is given by hadronic exchanges. Thus, the goal is to solve the pentaquark BSE as a meson-baryon molecule that couples all relevant channels, using the same analytical tools as in the quark-diquark case.

In this chapter, we present a description of our meson-baryon model, including the suitable particles to form the proper quark content ($c\bar{c}duu$). Also, we establish the bosons that can be exchanged. The expressions for the kernels and propagators are provided along with a brief description of solution techniques for the corresponding BSE (details can be found in Chapter 4).

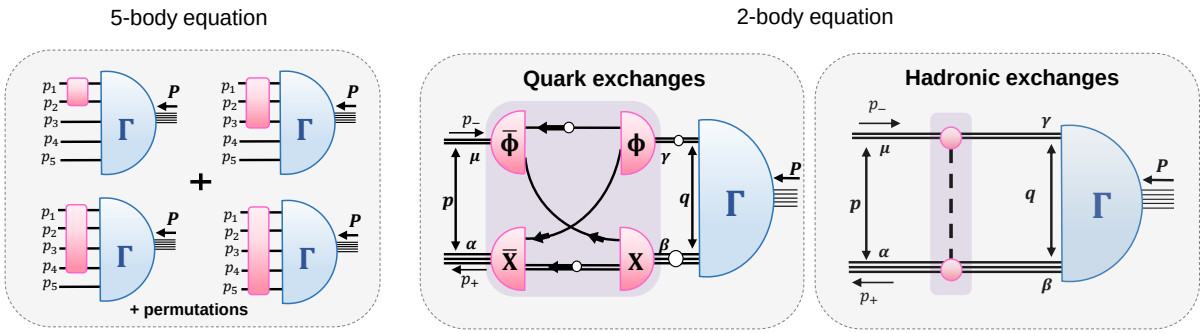

Figure 3.1: Schematic representation of the possible pentaquark pictures: 5-body system (*left*), and meson-baryon configurations with quark exchanges (*middle*) or hadronic exchanges (*right*). The latter is the model used in our calculations.

3.1 Meson-baryon "molecule"

In our calculations, we consider the simplest case, namely a meson-baryon molecule bound together by hadronic exchanges, particularly a one-boson exchange (Figure 3.1 - *right*). Also, we approximate the propagators, whose most general structure (eq. (2.23)) is derived from Lorentz invariance, by free propagators. As an example, a baryon propagator has the same structure as the quark propagator since both are fermions, so they have the same symmetries; the vector-meson propagator has the same structure as the gluon propagator, etc. The structure of the meson-baryon vertices is also determined by Lorentz invariance, and they are given below.

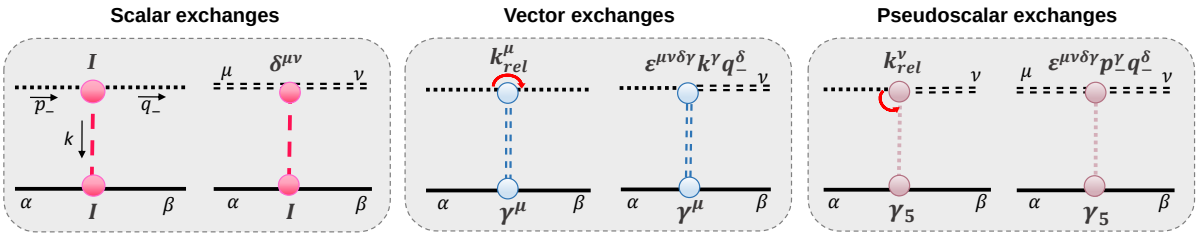

Figure 3.2: Interaction kernels for scalar (*left*), vector (*middle*), and pseudoscalar (*right*) exchange bosons. The vertices are proportional to the tensorial structures in the Figure. The solid lines represent baryons, double dashed lines vector mesons, and dotted lines stand for pseudoscalar mesons. The momenta in every diagram flow in the same way as depicted in the diagram on the left. The red arrows represent the relative momentum between the two pseudoscalar mesons, defined as $k^{\mu}_{rel} = (k_{in} + k_{out})/2$, where in and out denote the ingoing and outgoing momentum, respectively.

3.1.1 Propagators, kernels, and vertices

The meson and baryon propagators are taken to be free propagators. The pseudoscalar-meson, vector-meson and baryon propagators are then given by

$$D_P(q) = \frac{1}{q^2 + M_P^2}\,, \quad D_V^{\mu\nu}(q) = \frac{1}{q^2 + M_V^2}\,T_q^{\mu\nu}, \quad S(q) = \frac{-i\not{q} + M_b^2}{q^2 + M_b^2}\,, \tag{3.1}$$

where q is the momentum of the particle, M is the mass, and $T_q^{\mu\nu} = \left(\delta^{\mu\nu} - \frac{q^\mu q^\nu}{q^2}\right)$ is the transverse projector.

The vertex interactions have to conserve the quantum numbers, including, for example, spin and isospin. Consequently, the exchanged particles have to be bosons to conserve spin and their quark content has to be $\bar{q}q$, with $q = u, d$ or c to conserve isospin and be color neutral. Lastly, depending on the spin of the meson considered in the molecule, the exchanged mesons can be scalar, pseudoscalar or vector. The vertex structures are given in Figure 3.2.

Each vertex has an associated coupling constant, denoted by $\alpha_i, i = 1, 2$, where 1 stands for the baryon-boson interaction and 2 for the meson-boson one. The coupling constants enter the kernel, and they measure the strength of that individual interaction. In our simple model, these couplings are

assumed to be equal in all vertices. Ideally, the couplings' values could be calculated self-consistently from QCD through the construction of the relevant invariant transition matrix elements by mediating the transition between the three hadrons, for example by triangle diagrams on the vertices [49]. More details on how to calculate the coupling constants will be given in Chapter 5.

The interaction kernels are given by the product of the vertex tensors (Figure 3.2) and the scalar factor $1/(k^2 + m^2)$, where k is the momentum of the exchanged particle and m its mass. The one-boson-exchange kernels are written as:

Scalar exchanges:

$$K_{PP}(k) = \alpha\, I\, \frac{1}{k^2 + m^2}\ , \quad K^{\mu\nu}_{VV}(k) = \alpha\, I\, \frac{\delta^{\mu\nu}}{k^2 + m^2}\ , \tag{3.2}$$

Vector exchanges:

$$K_{PP}(k) = \alpha\, \frac{i\,\gamma^\mu\, k^\mu_{rel}}{k^2 + m^2}\ , \quad K^{\nu}_{PV}(k) = \alpha\, \epsilon^{\mu\nu\delta\gamma}\, \frac{\gamma^\mu k^\gamma\, q^\delta_-}{k^2 + m^2}\ , \tag{3.3}$$

Pseudoscalar exchanges:

$$K^{\nu}_{PV}(k) = \alpha\, \gamma_5 \frac{k^\nu_{rel}}{k^2 + m^2}\ , \quad K^{\mu\nu}_{VV}(k) = \alpha\, \epsilon^{\mu\nu\delta\gamma} \gamma_5 \frac{p^\gamma_-\, q^\delta_-}{k^2 + m^2}\ , \tag{3.4}$$

where the first superscript identifies the initial meson and the second the meson after the boson being exchanged. P means pseudoscalar and V vector meson, and α corresponds to the product of the coupling constants at each vertex, $\alpha = \alpha_1\alpha_2$. The momenta are defined in Figure 3.2.

The structure of the kernels where the vector meson after the exchange is converted into a pseudoscalar meson, K_{VP}, is the same as in the K_{PV} case. The only difference is in the relative momentum, which is always defined between the two pseudoscalar particles.

3.2 Coupled channel equation

Having established all ingredients beforehand - the propagators and kernels -, we are in a position to solve the Bethe-Salpeter equation that couples all relevant channels of the system. The resulting equation has the same structure as eq. (2.28). In this case S is the baryon propagator and the meson propagators (D) are defined in eqs. (3.1). The BSE is written as

$$\Gamma^\mu_a(p, P) = \int \frac{d^4q}{(2\pi)^4} \left\{ K^{\mu\nu}_{ab}(p, q)\, S_b(q_+)\, \Gamma^\gamma_b(q, P) \right\} D^{\nu\gamma}_b(q_-)\ , \tag{3.5}$$

where the index a stands for the initial channel and b for the intermediate state. We suppressed the Dirac indices for simplicity. The indices μ, ν and γ are the Lorentz indices, where we combine pseudoscalar and vector constituents into Lorentz indices $\mu = 0 \ldots 4$. $p_\pm$ are the external momenta of the propagators and $q_\pm$ are the internal momenta defined as $q_- = q + \eta P$ and $q_+ = q - (1 - \eta)P$, with η being the momentum partitioning parameter (details in Appendix A.1).

The pseudoscalar meson propagator corresponds to the scalar amplitude with Lorentz index $\mu = 0$, and the vector meson produces the vector amplitudes with $\mu = 1...4$. As an example, K_{PP} coincide with K^{00} in the Lorentz index notation, and K_{PV} corresponds to $K^{0\nu}$. For the propagator, we can only have D_{PP}, and D_{VV}; D^{00} for the pseudoscalar propagator and $D^{\mu\nu}$ for the vector propagator. There are no mixed propagators D_{PV} or D_{VP}. The coupled eq. (3.5) is schematically represented in Figure 3.3.

To solve the coupled BS equation and obtain the masses of the possible bound states, one has to calculate the full kernel matrix that includes all channels and exchanged particles. In other words, one calculates the kernel for each channel and sums over all exchanged particles, and then all channels contribute to the final amplitude. Each channel has the structure depicted in Figure 3.3 - *right*. After calculating the full matrix, we solve the equation as an eigenvalue problem, where the eigenvectors are the amplitudes $\Gamma^{\mu}(p, P)$. The detailed solution method is presented in Chapter 4.

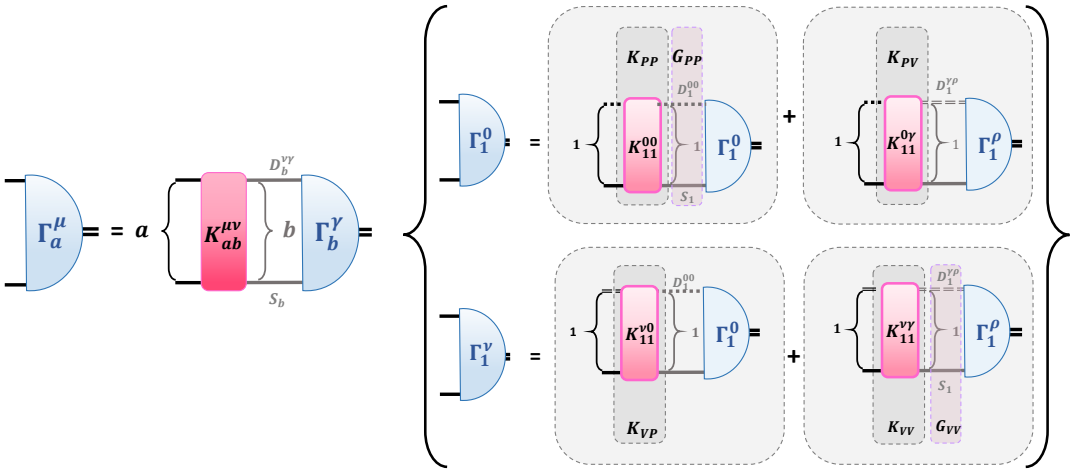

Figure 3.3: Representation of the coupled channel equation (3.5) (*left*). Example of the amplitudes, kernels, and propagators in the case where channels indices are both one ($a = b = 1$). There are four possible kernels depending on the mesons, but only two propagators. The lines means the same as in Figure 3.2. The sum over the exchanged particles is implicit (*right*).

3.2.1 Pentaquark system

As discussed in the previous sections, we model the pentaquark by a meson-baryon molecule and include all channels that can form a $c\bar{c}uud$ content. There are two possible combinations for the initial and final states:

$$(c\bar{c}) + (qqq) \quad \text{or} \quad (\bar{c}q) + (cqq)\ ,$$

where q means a light quark, u or d, which are the same since we assume isospin symmetry, and c is a charm quark. These two possibilities for the molecular configurations are given in Figure 1.1. For instance, a possible molecule is formed by the meson $D\,(\bar{c}q)$ and the baryon $\Sigma_c\,(cqq)$. For the exchanged particles, we consider the light mesons σ, ρ and π ($\sim \bar{q}q$), and the charmed mesons $\overline{D}$ and $\overline{D}^*\,(\bar{c}q)$.

The possible channels and exchanged particles are presented in Figure 3.4, where the coupled channel equation represented in Figure 3.3 describes each channel for a particular value of the indices a and b. The full kernel matrix for the pentaquark system is given by the combination of all channels and the sum over all exchanged particles in Figure 3.4. A list of these particles, including masses and quantum numbers is given in Appendix B.

The interactions between $\eta_c p$ and $J/\psi p$ $(a = 2, b = 2)$ are suppressed since light quarks can only couple to c via quark-disconnected (and thus OZI-suppressed) diagrams, which is the reason why they are not considered in our calculations. However, other channels can fluctuate into these through two-loop diagrams justifying why even though the $\eta_c p$ and $J/\psi p$ thresholds are lower, they are not the dominant contributions to the pentaquark states. The $\Lambda_c \overline{D}$ system has the suitable quark content to form a pentaquark state, however it was found to be repulsive [31].

The natural quantum numbers for bound states made of $J^P = \frac{1}{2}^+$ baryons (Σ_c, p) and mesons with $J^P = 0^-$ $(\overline{D}, \eta_c)$ or 1^- $(\overline{D}^*, J/\psi)$ are $J^P = \frac{1}{2}^-$ and $\frac{3}{2}^-$. In the following we only consider the $\frac{1}{2}^-$ case, for simplicity.

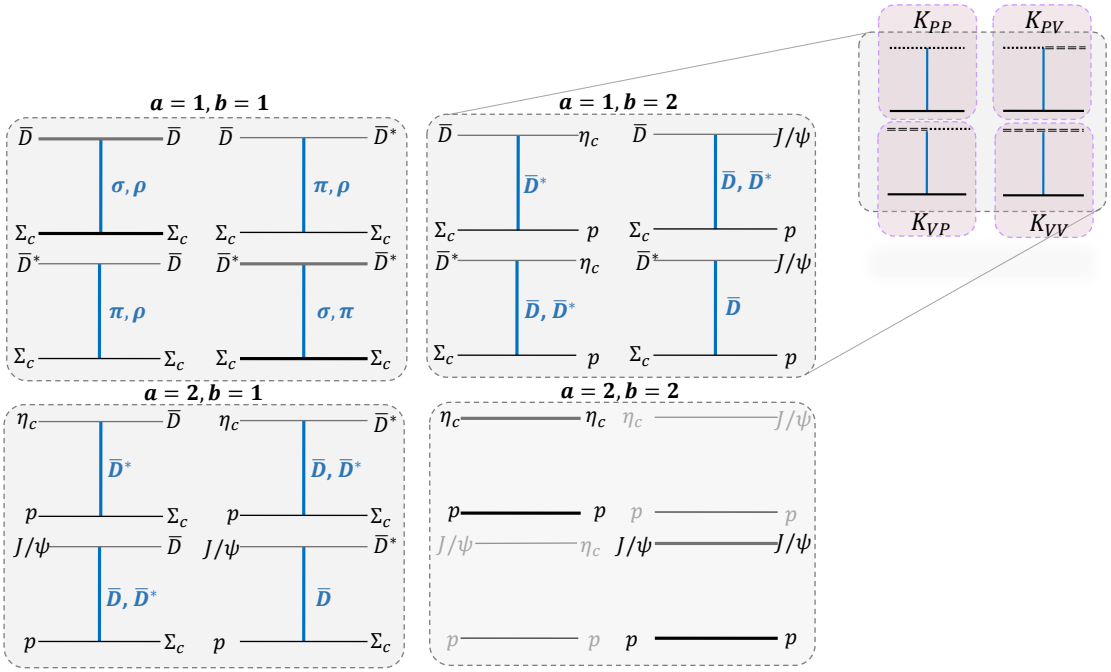

Figure 3.4: Possible channels and exchanged particles for the pentaquark system. Gray solid lines represent a general meson and solid black lines a fermion; the blue line is a generic interaction. Each one of the four channels in the main figure has the structure represented on the top scheme, where the meson propagator lines follow the same notation as in the previous figures.

Chapter 4

Numerical techniques

We want to solve a Bethe-Salpeter equation for a two-body system with $J^P = (1/2)^-$ with a one-boson exchange. To solve the BSE, we expand the BS amplitude and the wave functions in terms of Dirac basis elements with Lorentz invariant dressing functions. Afterwards, the Dirac and Lorentz contractions are performed independently in the equations for the BS amplitudes and BS wave functions together with a Chebyshev expansion for the angular variables. Then, the equation is converted into a matrix-vector multiplication, where the matrix is the product of the kernel and propagator matrices integrated over the momentum variable [47]. The eigenvectors correspond to the BS amplitudes $\Gamma^{\mu}_{a,\alpha\beta}(p,P)$.

For the purpose of checking our calculations, we solved the BSE for a fermion-scalar system, and we obtain the same results as in the Nakanishi method used in [50]. Even this simple model exhibits some undesirable features of unequal-mass/different-particle systems such as complex conjugate eigenvalues. Below, we present a technique to eliminate complex eigenvalues through the selection of the eigenvalues of the propagator matrix.

4.1 Method to solve the BSE

The equation we want to solve is the BSE for a two-body system, given in eq. (3.5), which couples the channels discussed in Chapter 3. We recall the equations:

$$\Gamma^{\mu}_{a,\alpha\beta}(p,P) = \int_q \left\{ K^{\mu\nu}_{ab}(p,q,P)\, S_b(q_+)\, \Gamma^{\gamma}_b(q,P) \right\}_{\alpha\beta} D^{\nu\gamma}_b(q_-) \ , \tag{4.1}$$

and

$$\chi^{\nu}_{b,\alpha\beta}(q,P) = \left\{ S_b(q_+)\, \Gamma^{\gamma}_b(q,P) \right\}_{\alpha\beta} D^{\nu\gamma}_b(q_-) \ , \tag{4.2}$$

where $\int_q \equiv \frac{1}{(2\pi)^4} \int_0^\infty dq\, q^3 \int_{-1}^1 dz' \sqrt{1-z'^2} \int_{-1}^1 dy \int_0^{2\pi} d\psi$, and P is the total momentum of the state (all four-momentum vectors are explicitly given in the Appendix A.2). The angular integration on ψ is trivially 2π, the angular variable z' is defined as $z' = \hat{q} \cdot \hat{P}$, where the " $\hat{}$ " is the normalized momentum (for instance, $\hat{p} = p/\sqrt{p^2}$), and the variable y is given by $y = \hat{p}_\perp \cdot \hat{q}_\perp$, where the transverse momentum is defined as $\hat{p}_\perp = \hat{p} - (\hat{p} \cdot \hat{P})\, \hat{P} = \hat{p} - z\, \hat{P}$, and z is $z = \hat{p} \cdot \hat{P}$. The indices α and β are the Dirac indices

of the baryon and the pentaquark. $\chi^{\nu}_{b\,\alpha\beta}(q,P)$ is the BS wave function. The equation is schematically depicted in Figure 4.1.

We start by working out the BSE for the first channel $(\Sigma_c\{\overline{D},\overline{D}^*\} \leftrightarrow \Sigma_c\{\overline{D},\overline{D}^*\})$, only. The structure of the kernels and propagators is the same for each channel; hence, in the following equations the channel indices are omitted. Furthermore, we assume that the exchanged particles have already been summed up when the coupling constant $\alpha_{ab,\text{ex}}$ is multiplied in the kernel with the factor $1/(k^2+m^2)$, which is the only quantity that depends on the exchanged particle. The coupling constants are the parameters that allow one to switch off/on channels and exchanged particles. Thus, the following kernel matrices result from all particles that can be exchanged in a particular channel.

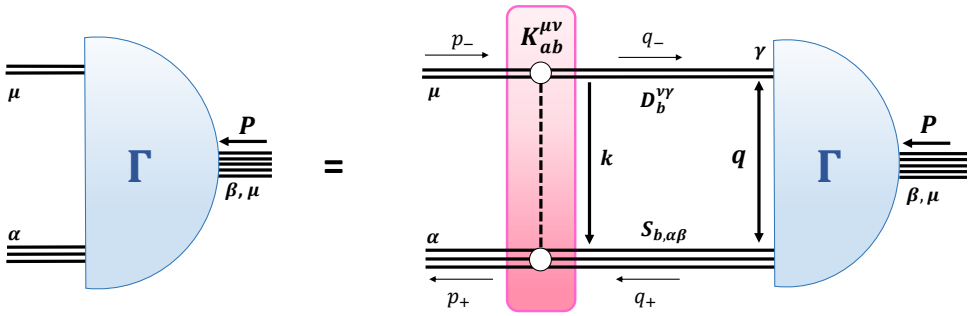

Figure 4.1: Pictorial representation of the BSE given in Eq. (4.1).

We have to calculate five different amplitudes corresponding to the five Lorentz indices, the peudoscalar ($\mu = 0$) and vector ($\mu = 1\ldots4$) amplitudes, respectively, given by:

$$\begin{aligned}\Gamma^{0}_{\alpha\beta}(p,P) &= \int_q \left\{K^{00}\,(p,q,P)\,\chi^{0}(q,P) \;+\; K^{0\nu}\,(p,q,P)\,\chi^{\nu}(q,P)\right\}_{\alpha\beta}\,,\\ \Gamma^{\mu}_{\alpha\beta}(p,P) &= \int_q \left\{K^{\mu 0}\,(p,q,P)\,\chi^{0}(q,P) \;+\; K^{\mu\nu}\,(p,q,P)\,\chi^{\nu}(q,P)\right\}_{\alpha\beta}\,,\end{aligned} \tag{4.3}$$

where K^{00} corresponds to K_{PP}, $K^{0\nu}$ is the K^{μ}_{PV}, $K^{\mu 0}$ is K^{μ}_{VP}, and $K^{\mu\nu}$ corresponds to $K^{\mu\nu}_{VV}$ in the notation of Figure 3.4.

Besides, we also divide the wave function into a scalar and vector part,

$$\begin{aligned}\chi^{0}_{\alpha\beta}(q,P) &= \left\{S(q_+)\,\Gamma^{0}(q,P)\right\}_{\alpha\beta} D^{00}(q_-)\,,\\ \chi^{\nu}_{\alpha\beta}(q,P) &= \left\{S(q_+)\,\Gamma^{\mu}(q,P)\right\}_{\alpha\beta} D^{\mu\nu}(q_-)\,,\end{aligned} \tag{4.4}$$

where D^{00} corresponds to the pseudoscalar meson propagator and $D^{\mu\nu}$ is the vector meson propagator.

Then, the BS amplitudes and the wave functions are expanded into Lorentz scalar functions f_i and g_i, and Dirac basis elements $\tau^{\mu}_{i,\alpha\beta}$:

$$\Gamma^\mu_{\alpha\beta}(p,P) = \sum_{i=1}^{8} f_i(p^2,z,P^2)\,\tau^\mu_{i,\alpha\beta}(p,P)\,,$$
$$\chi^\mu_{\alpha\beta}(q,P) = \sum_{j=1}^{8} g_j(q^2,z',P^2)\,\tau^\mu_{j,\alpha\beta}(q,P)\,. \tag{4.5}$$

There are eight basis elements, where the first two describe the Dirac and Lorentz structure of the pseudoscalar part and the rest the vector part. The Dirac basis elements result from a particular representation of the symmetry properties of the state under parity and spin. For numerical convenience, one uses an orthonormal basis such that f_i and g_i are obtained directly by projection. The orthonormal basis, elements obey the following orthonormality property: $\frac{1}{2}\,\mathrm{Tr}\left\{\overline{\tau}^\mu_i(p,P)\,\tau^\mu_j(p,P)\right\} = \delta_{ij}$, where $\overline{\tau}^\mu_i(p,P)$ is the conjugate basis element, constructed in such a way that makes the basis orthonormal. Accordingly, there are eight Lorentz scalar functions f_i and g_i that depend on all possible Lorentz invariant momentum variables and inherit the symmetries of the amplitudes and wave functions. Therefore, the quantities Γ^μ and χ^μ are completely defined by these covariants. The basis elements are presented in Table 4.1.

$\Gamma^0(p,P)$	$\Gamma^\mu(p,P)$		
$\tau^0_1 = \frac{1}{\sqrt{2}}\Lambda_+$	$\tau^\mu_3 = \frac{1}{\sqrt{6}}\gamma_5\,\gamma^\mu_\perp\,\Lambda_+$	$\tau^\mu_5 = \frac{1}{4}i\gamma_5[\gamma^\mu_\perp, \widehat{\not{p}_\perp}]\Lambda_+$	$\tau^\mu_7 = \frac{1}{\sqrt{2}}i\gamma_5\,\widehat{\not{p}_\perp}^{\,\mu}\,\Lambda_+$
$\tau^0_2 = -i\,\widehat{\not{p}_\perp}\,\Lambda_+$	$\tau^\mu_4 = \frac{1}{\sqrt{2}}\gamma_5\hat{P}^\mu\Lambda_+$	$\tau^\mu_6 = \frac{1}{\sqrt{2}}i\gamma_5\hat{P}^\mu\widehat{\not{p}_\perp}\,\Lambda_+$	$\tau^\mu_8 = \frac{2}{\sqrt{3}}\gamma_5(\widehat{\not{p}_\perp}^{\,\mu}\widehat{\not{p}_\perp} - \frac{1}{3}\gamma^\mu_\perp)\Lambda_+$

Table 4.1: Orthonormal basis elements for the meson-baryon BS amplitudes with $J^P = (1/2)^-$. The transverse momentum is abbreviated by $\hat{p}_\perp = \hat{p} - z\hat{P}$, and the transverse normalized momentum by $\widehat{\not{p}_\perp} = (\hat{p} - z\hat{P})/\sqrt{1-z^2}$. $\gamma^\mu_\perp$ represents the transverse γ matrices $\gamma^\mu_\perp = T^{\mu\nu}_p\gamma^\nu$. Λ_+ is the positive-energy projector, whose P dependence is suppressed for brevity.

Now, we apply the basis projection to the BS amplitude $\Gamma^\mu(p,P)$ defined in eq. (4.1) In this way, we obtain the dressing functions of the BS amplitude:

$$\begin{aligned} f_i(p^2,z,P^2) &= \int_q \sum_j g_j(q^2,z'^2,P^2)\,\frac{1}{2}\mathrm{Tr}\left\{\overline{\tau}^\mu_i(p,P)\,K^{\mu\nu}(p^2,q^2,P^2)\,\tau^\nu_j(q,P)\right\} \\ = \int_q \sum_j g_j(q^2,z',P^2)\,\Bigg(&\underbrace{\frac{1}{2}\,\mathrm{Tr}\left\{\overline{\tau}^0_i(p,P)\,K^{00}(p^2,q^2,P^2)\,\tau^0_j(q,P)\right\}}_{K^{PP}_{i=1,2;\,j=1,2}(p^2,q^2,z,z',y,P^2)} + \underbrace{\frac{1}{2}\,\mathrm{Tr}\left\{\overline{\tau}^0_i(p,P)\,K^{0\mu}\,\tau^\mu_j(q,P)\right\}}_{K^{PV}_{i=3\ldots8;\,j=1,2}(p^2,q^2,z,z',y,P^2)} \\ &+ \underbrace{\frac{1}{2}\,\mathrm{Tr}\left\{\overline{\tau}^\mu_i(p,P)\,K^{\mu 0}(p^2,q^2,P^2)\,\tau^0_j(q,P)\right\}}_{K^{VP}_{i=3\ldots8;\,j=1,2}(p^2,q^2,z,z',y,P^2)} + \underbrace{\frac{1}{2}\,\mathrm{Tr}\left\{\overline{\tau}^\mu_i(p,P)\,K^{\mu\nu}(p^2,q^2,P^2)\,\tau^\nu_j(q,P)\right\}}_{K^{VV}_{i=3\ldots8;\,j=3\ldots8}(p^2,q^2,z,z',y,P^2)}\Bigg). \end{aligned} \tag{4.6}$$

The basis expansion results into an 8×8 matrix (represented in Figure 4.2) that corresponds to the distinct kernels of each channel. For instance, in Figure 3.4, the kernel of the $\Sigma_c\overline{D} - \Sigma_c\overline{D}$ diagram of the first channel ($a = b = 1$) corresponds to K^{PP}_{ij}, where $i,j = 1,2$ since the meson $\overline{D}$ is a pseudoscalar

meson, while the kernel of the second diagram $\Sigma_c\overline{D} - \Sigma_c\overline{D}^*$ is K_{ij}^{PV}, where $i = 1, 2;\ j = 3...8$ since the meson $\overline{D}^*$ is a vector.

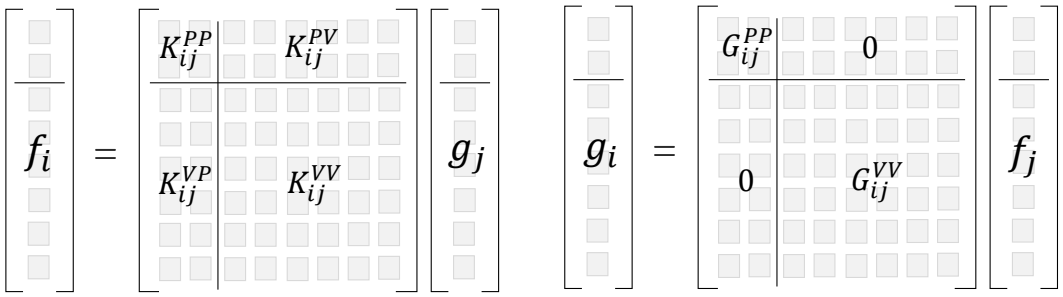

Figure 4.2: Kernel and propagator matrices that result from the basis expansion. The first two elements in f_i and g_i correspond to the scalar amplitude and pseudoscalar propagator, respectively. The remaining six describe the vector part. Since there are no mixed propagators, the off-diagonal elements of the G_{ij} matrix are zero. Each small gray square is a matrix, whose dimension depends on the number of quadrature grid points.

In the next steps, we will make the dependence on the continuous momentum and angular variables numerically accessible. To accomplish this, we apply the Gauss-Legendre quadrature method, which replaces an integral with a sum over the integrand evaluated at certain points times their weights [51]. For example, since only the kernel K_{ij} depends on the variable y, we can already perform this integration in the following way:

$$K_{ij}(p^2, q^2, z, z', P^2) = \int dy\, K_{ij}(p^2, q^2, z, z', y, P^2) = \sum_s^{n_y} K_{ij}(p^2, q^2, z, z', y_s, P^2)\, w[y_s]\,, \tag{4.7}$$

where n_y is the number of grid points for the variable y, s identifies the quadrature point and $w[y_s]$ its weight. This is the general expression of the quadrature method, which discretizes a continuous variable to replace the integral by a sum, allowing for numerical computation.

Then, one implements the expansion in eq. (4.5) to $\chi^{\mu}_{\alpha\beta}(q, P)$ in equation (4.2) to obtain the BS wavefunctions components:

$$\begin{aligned} g_i(q^2, z', P^2) &= \sum_j f_j(p^2, z, P^2)\, \frac{1}{2}\, \mathrm{Tr}\left\{\, \overline{\tau}_i^{\mu}(q, P)\, S(q_+)\, \tau_j^{\nu}(q, P)\right\} D^{\mu\nu}(q_-) \\ &= \sum_j f_j(p^2, z, P^2) \Bigg(\underbrace{\frac{1}{2}\, \mathrm{Tr}\left\{\overline{\tau}_i^{0}(q, P)\, S(q_+)\, \tau_j^{0}(q, P)\right\}}_{G^{PP}_{i=1,2;\, j=1,2}(q^2, z', P^2)}\, D^{00}(q_-) \\ &\qquad + \underbrace{\frac{1}{2}\, \mathrm{Tr}\left\{\overline{\tau}_i^{\mu}(q, P)\, S(q_+)\, \tau_j^{\nu}(q, P)\right\}}_{G^{VV}_{i=3\ldots8;\, j=3\ldots8}(q^2, z', P^2)}\, D^{\mu\nu}(q_-) \quad . \end{aligned} \tag{4.8}$$

In the same way as the kernel, the expansion results into an 8×8 matrix (represented in Figure 4.2)

that corresponds to each channel's propagators. There are no mixed propagators, so one only has the baryon by pseudoscalar meson propagator product, given by G_{ij}^{PP}, and the product of the baryon by the vector meson, written as G_{ij}^{VV}. For instance, $\Sigma_c\overline{D}$ corresponds to G_{ij}^{PP}, where $i,j=1,2$ since $\overline{D}$ is a pseudoscalar meson, and $\Sigma_c\overline{D}^*$ to G_{ij}^{VV}, where $i,j=3...8$ since $\overline{D}^*$ is a vector meson.

For later convenience, we expand the kernel K_{ij} and the propagator G_{ij} into Chebyshev polynomials of the second kind which hold the dependence on the angular variables z and z' (see details in Appendix A.3). Applying the expansion to the kernel and propagator matrices in eqs. (4.6) and (4.8) leads to:

$$\begin{aligned} f_i(p^2,z,P^2) &= \int_q \sum_{jn} g_j(q^2,z',P^2)\, K_{ij}(p^2,q^2,z,z',P^2) \\ \Rightarrow f_{im}(p^2,P^2) &= \int_q \sum_{jn} g_{jn}(q^2,P^2) \underbrace{\int dz\, \Omega(z)\, \Omega(z')\, Y_m^*(z)\, Y_n(z')\, K_{ij}(p^2,q^2,z,z',P^2)}_{K_{ijmn}(p^2,q^2,P^2)}\,, \end{aligned} \tag{4.9}$$

$$\begin{aligned} g_i(q^2,z',P^2) &= \sum_{jn} f_j(q^2,P^2)\, G_{ij}(q^2,z',P^2) \\ \Rightarrow g_{im}(q^2,P^2) &= \sum_{jn} f_{jn}(q^2,P^2) \underbrace{\int dz'\, \Omega(z')\, Y_m^*(z')\, Y_n(z')\, G_{ij}(q^2,z',P^2)}_{G_{ijmn}(q^2,P^2)}\,, \end{aligned} \tag{4.10}$$

where $Y_m(z)$ is the Chebyshev polynomial of order m, and $\Omega(z)$ and $\Omega(z')$ are the integration weights.

Thereafter, the full matrix is calculated by multiplying the kernel and the propagator matrices, and the integration over the momentum variable leads to the following equation:

$$f_{im}(p^2,P^2) = \sum_{jnkr} \underbrace{\int dq^2\, K_{ikmr}(p^2,q^2,P^2)\, G_{kjrn}(q^2,P^2)}_{\mathbf{K}^{\mathcal{Q}}_{ijmn}(P^2)}\, f_{jn}(q^2,P^2)\,, \tag{4.11}$$

where $\mathbf{K}^{\mathcal{Q}}_{ijmn}(P^2)$ is the full kernel matrix that defines each channel. The index $\mathcal{Q}$ stand for the discretized momentum dependence. The dimension of the matrix $K^{\mathcal{Q},ab}_{ijmn}(p^2,P^2)$ is given by $(n_p \times n_{cheb} \times n_{ch} \times 8,\, n_p \times n_{Cheb} \times n_{ch} \times 8)$, where n_p represents the number of grid points to calculate the integration in the radial variable p, n_{Cheb} is the number of Chebyshev moments, 8 is the number of basis elements and n_{ch} is the number of channels.

Finally, having calculated the full kernel for each channel, one can sum over the indices of the final channel b, by transforming the system into a matrix-vector multiplication. An artificial eigenvalue $\lambda(P^2)$ is introduced and the eigenvectors F represent the BS amplitude $\Gamma^{\mu}_{a,\alpha\beta}(p,P)$. The equation is

$$F^a_{im} = K^{\mathcal{Q},ab}_{ijmn}(P^2)\, F^b_{jn} \;\;\Rightarrow\;\; \lambda(P^2)\, F^a_{im} = K^{\mathcal{Q},ab}_{ijmn}(P^2)\, F^b_{jn}\,, \tag{4.12}$$

To find a bound state solution, we vary P^2 to identify the values where some of the eigenvalues become one, which then corresponds to the mass of a possible bound state. More efficiently, we calculate the kernel with all coupling constants equal to 1. Thus for any P^2, the inverse eigenvalues $1/\lambda(P^2)$ is a value of a common coupling constant c, by which we can multiply the kernel to produce a bound state.

The smallest corresponds to a ground state's mass and the larger ones to possible excited states.

4.2 Fermion-Scalar Model

To compare with the literature, we solved a BSE for a fermion-scalar system with $J^P = (1/2)^+$ for a scalar and a vector particle being exchanged. Even this simple system exhibits some typical features of BSEs for unequal particles, like the complex conjugate eigenvalues that occur already in scalar theories as an interference of normal and "abnormal" states [52, 53]. Furthermore, this model was used as a check for our calculations, and indeed we reproduce the results of Nogueira *et al.* [50], where the same system is solved through another method - the Nakanishi weight functions method.

The kernel is given by K_{PP} in eqs. (3.2) and (3.3) in the scalar and vector case, respectively. The propagators are equal to the ones defined in eq. (3.1). The basis elements applied are the same as in Table 4.1, because a fermion-pseudoscalar system with parity $-$ is equivalent to a fermion-scalar system with parity $+$.

The equation is solved for equal masses of the fermion and scalar or vector particles m, and the mass of the exchanged particles is $\mu = 0.5\,m$ in the scalar case, and $\mu = 0.15\,m$ for the vector exchange. Our results for the scalar and vector cases, as well as those of [50], are plotted in Figure 4.3.

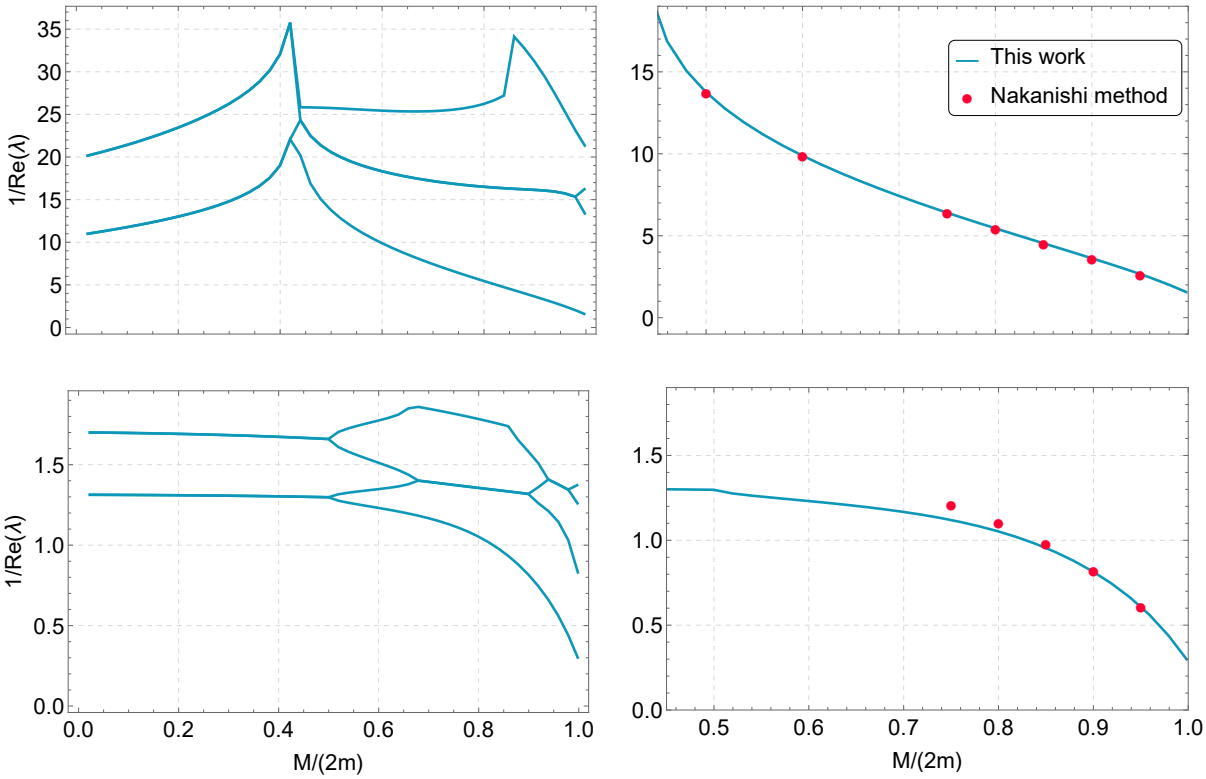

Figure 4.3: *Left:* Inverse eigenvalue spectrum for the scalar-fermion system with a scalar (*top*) and vector (*bottom*) exchange, respectively. In the right panels, we zoom in the lowest eigenvalue (blue line) and compare with the Nakanishi method [50] (pink circles) for scalar and vector exchange.

4.2.1 Complex conjugate eigenvalues

Because the interaction meets a difficulty in binding the system, complex eigenvalues appear; they correspond to the crossing of a physical with an unphysical solution [53]. Unphysical solutions may arise as an artifact of the truncation, for example in an inconsistent combination of a ladder truncation with a tree-level propagator. With more realistic kernels, they would presumably vanish.

For physical constituents and a massless exchange particle, when $P^2 \to (m_1 + m_2)^2$, with m_1 and m_2 being the masses of the particles, the inverse eigenvalues vanish, but this does not happen in the unphysical states since they do not cross the coupling constant value at any point.

For a given bound state, the eigenvalue spectrum should be real if KG is hermitian. However, because this is not necessarily the case, we employ a method that resolves the problem, which we describe in the following.

4.2.2 Eigenvalue reconstruction

The kernel K and the propagator G matrices are both hermitian, but $(KG) \neq (KG)^\dagger$ because they do not commute. For unequal masses, solutions with different type of eigenvalues may interfere, and this could be the underlying mechanism for the generation of complex eigenvalues [52].

- **$\mathbf{K}$ and $\mathbf{G}$ real and symmetric:** In principle, the kernel and the propagator matrices can always be transformed into real and symmetric matrices: $G_{mn}(p^2, P^2) = G_{nm}(p^2, P^2)$ and $K_{mn}(p^2, p'^2, P^2) = K_{nm}(p'^2, p^2, P^2)$. Initially, due to choices of particular bases and polynomials, the matrix entries can be real or imaginary, so we perform the following transformation to make K and G real and symmetric,

$$K\,G\,\Gamma_i = \lambda_i \Gamma_i \to \underbrace{(hKg)}_{\text{real and}}\ \underbrace{(g^\dagger G h^\dagger)}_{\text{symmetric}} (h\Gamma_i) = \lambda_i\,(h\Gamma_i)\,, \tag{4.13}$$

  where g and h are diagonal matrices with entries 1 or i.

- **$\mathbf{G}$ positive or negative:** If K and G are real and symmetric, then from a Cholesky decomposition one shows that KG is hermitian if $G > 0$ or $G < 0$. So, performing a spectral decomposition of the propagator matrix from its eigenvalues η_i and eigenvectors ξ_i gives:

$$G\,\xi_i = \eta_i \xi_i \to G' = \sum_{\eta_i > 0 \text{ or } \eta_i < 0} \eta_i\,\xi_i \xi_i^\dagger\,, \tag{4.14}$$

  leading to a new equation with different eigenvalues λ_i':

$$K\,G'\,\Gamma_i' = \lambda_i'\,\Gamma_i'\,. \tag{4.15}$$

  Because $K\,G'$ is hermitian, λ_i' must be real and the Γ_i' are orthogonal.

This restriction of the propagator matrix to its positive or negative eigenvalues disentangles the complex eigenvalues of the BSE to become real and exhibit only the characteristics of physical or unphysical solutions.

The eigenvalue reconstruction for the fermion-scalar case is shown in Figure 4.4 as well as the reconstructed eigenvectors that correspond to the Bethe-Salpeter amplitudes.

In order to implement the reconstruction numerically, once the final propagator matrix G_{ijmn} in equation (4.10) is obtained, one calculates its eigenvalues and eigenvectors. Then, we select either the positive or the negative eigenvalues and reconstruct the propagator matrix according to equation (4.14). Afterwards, we proceed as previously described, by using the reconstructed propagator matrix for solving the BSE and calculate its eigenvalues and eigenvectors.

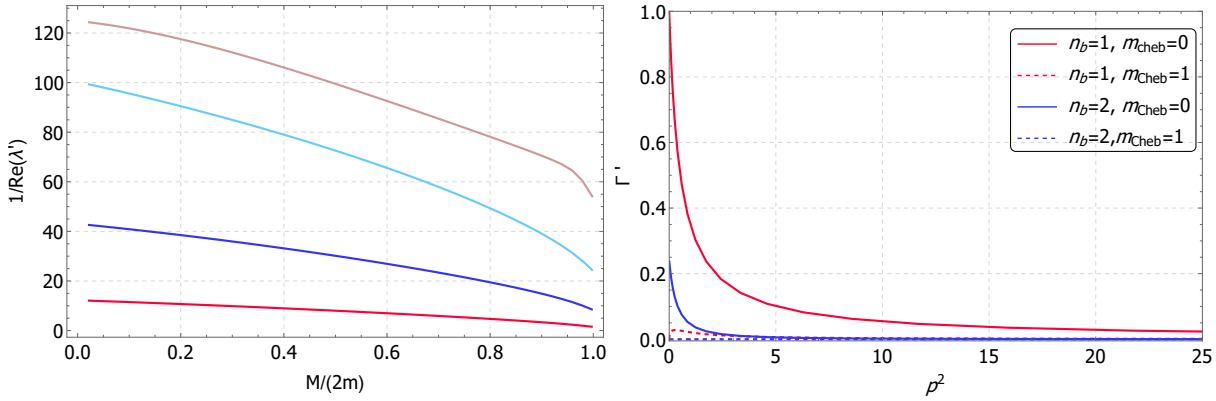

Figure 4.4: Inverse eigenvalue reconstruction for the fermion-scalar system with a scalar exchange (represented in Figure 4.3 - *top left*), keeping the positive eigenvalues of the propagator matrix (*left*) and the respective eigenvectors (*right*). $n_b = 1$ or $n_b = 2$ labels the basis element and $m_{Cheb} = 0, 1$ the Chebyshev moment.

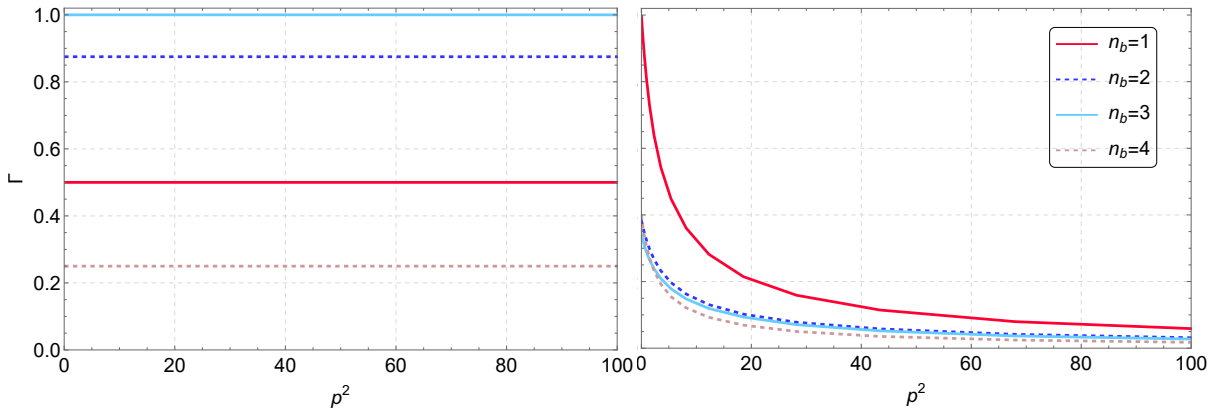

Figure 4.5: BS amplitudes without (*left*) and with (*right*) the monopole form factor given in eq. (4.16), with $\alpha = 1$ and $\Lambda = 1$ GeV. These amplitudes correspond to all channels and exchanged particles switched on (see Figure 3.4). We only plot $n_b = 1$ to 4 with $m_{Cheb} = 0$ for the ground state as an example.

4.3 Suppression form factor

In order to make the loop integrals converge, we had to include a form factor in the kernels of eqs. (3.2), (3.3) and (3.4), ensuring that the BS amplitudes fall off for large momenta. This factor is given by:

$$F(q^2, \Lambda^2) = \frac{\Lambda^2}{(\Lambda^2 + q^2)^{\alpha}} , \quad \alpha = 1, 2 , \tag{4.16}$$

where Λ is the cutoff value and q is the relative internal momentum between the two constituent particles. $\alpha = 1$ corresponds to a monopole and $\alpha = 2$ to a dipole form factor. This suppression factor is also used in other models [34, 54, 55]. Before introducing this factor, the amplitudes are constant for all p^2 values, as depicted in Figure 4.5 - *left*.

We tested how different values of Λ and α influence the eigenvalue spectrum and amplitudes. These tests were made for all channels switched on (in Figure 3.4), and they are depicted in Figures 4.6 and 4.7.

Comparing both spectra in Figure 4.6, one concludes that using a dipole instead of a monopole form factor mostly re-scales the spectrum. When using a dipole, the inverse eigenvalues increase their magnitude with respect to the spectrum produced with a monopole form factor; however, the eigenvalues' fundamental shape is basically maintained. In our subsequent calculations, we chose the monopole form factor.

Afterwards, we tested several cutoff values for the monopole form factor. Besides $\Lambda = 1$ GeV, depicted in Figure 4.6 - *left*, we calculated the results for Λ = 0.5, 2, 3 and 5 GeV. We conclude that increasing the cutoff value decreases the magnitude of the inverse eigenvalues, but at the same time, they become flattened. In the cases where the cutoff is 2, 3, or 5 GeV, some inverse eigenvalues turn into a constant, and they should decrease towards the threshold region. Thus, we are left with Λ= 0.5 and 1 GeV. Since both eigenvalue spectra show the expected behavior, but when Λ = 1 GeV, the inverse eigenvalues are lower, we stick with that choice.

Having chosen the monopole form factor (α = 1) and Λ = 1 GeV, we plot the amplitudes in Figure 4.5 - *right* and verify that they have the correct behavior, decreasing for large p^2 values.

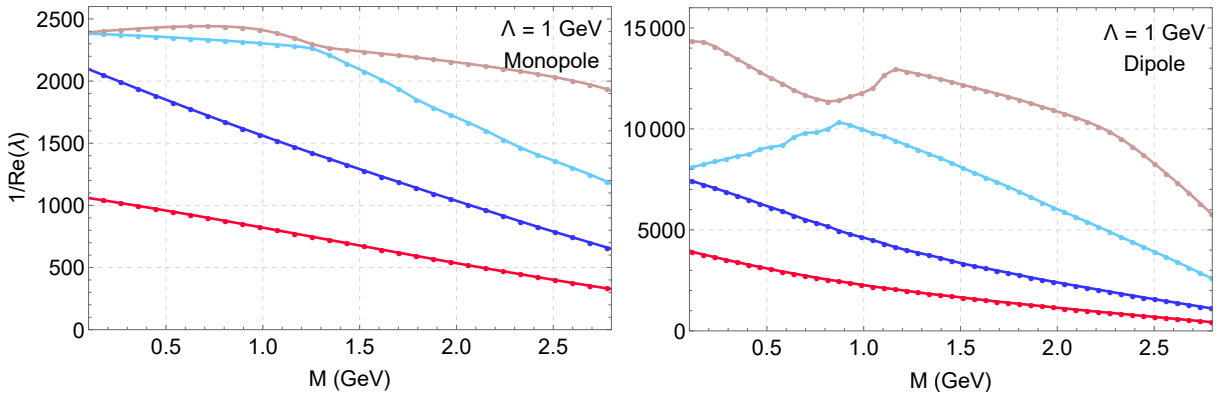

Figure 4.6: Inverse eigenvalue spectrum for all diagrams from both channels switched on, including a monopole (*left*) and a dipole form factor (*right*). The cutoff value is fixed to 1 GeV.

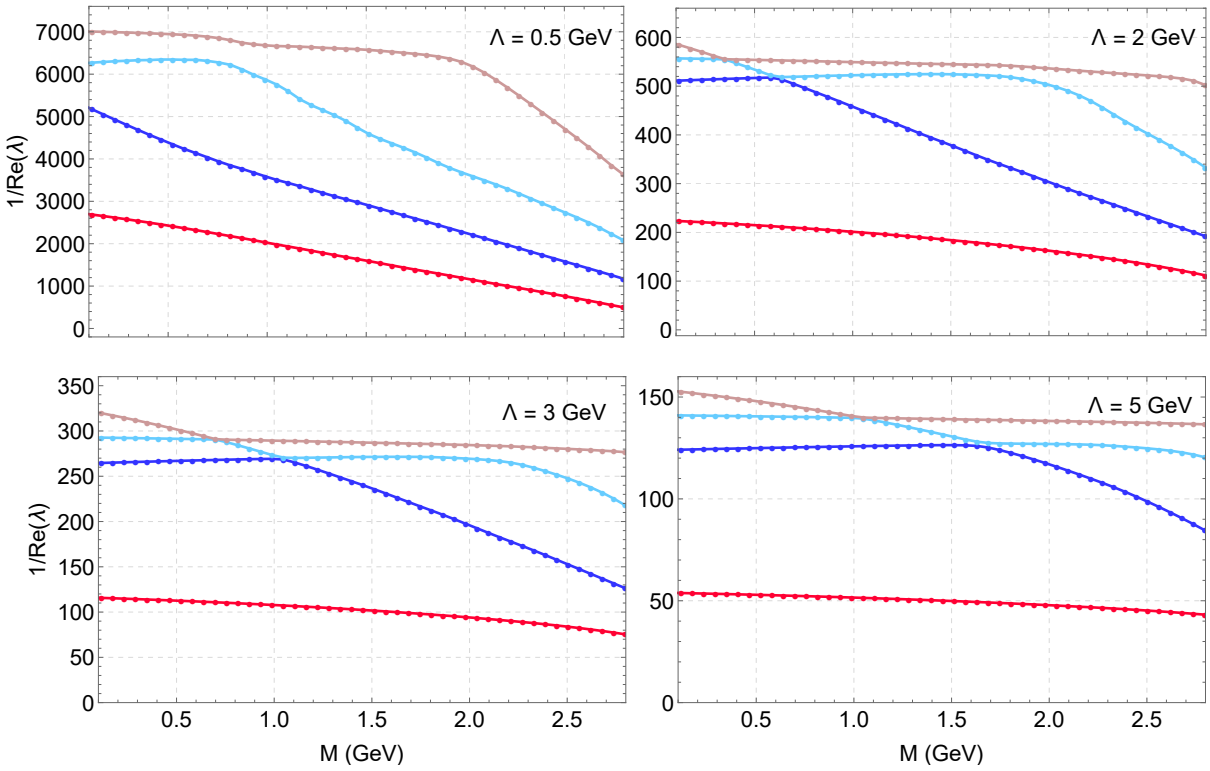

Figure 4.7: Inverse eigenvalue spectrum for all diagrams from the two channels switched on, including a monopole form factor for several values of the cutoff Λ.

4.4 Integral convergence

For the purpose of determining the number of grid points to implement in our calculations, we performed some convergence tests in the integration variables p, y, z and in the order of the expansion variable n_{Cheb} to verify the minimal number of points to ensure convergence in the results, using as little as possible computational time and memory.

Our results are represented in Figure 4.8, where we tested three values for each variable. In the top panels, one sees that the number of p and y points does not change the result considerably. On the momentum variable p and on variable y, the relative error between the three values nearest to the threshold is less than 0.01%. Thus, in our calculations, we used the middle values, namely $n_p = 30$ which reduces the time needed to run the results and produces very similar numbers to the one with higher precision, and on y we employed 12 grid points. In the bottom panels, the relative error between $n_z = 16$ and the other cases is larger than 0.01%, so we employ 16 points in the angular variable z. On the Chebyshev polynomials order, the relative error between $n_{Cheb} = 8$ and $n_{Cheb} = 4$ or $n_{Cheb} = 6$ is respectively, larger and smaller than 0.01%, thus we use $n_{Cheb} = 6$. To sum up, in our calculations we employed $n_p = 30, n_y = 12, n_z = 16$ and $n_{Cheb} = 6$.

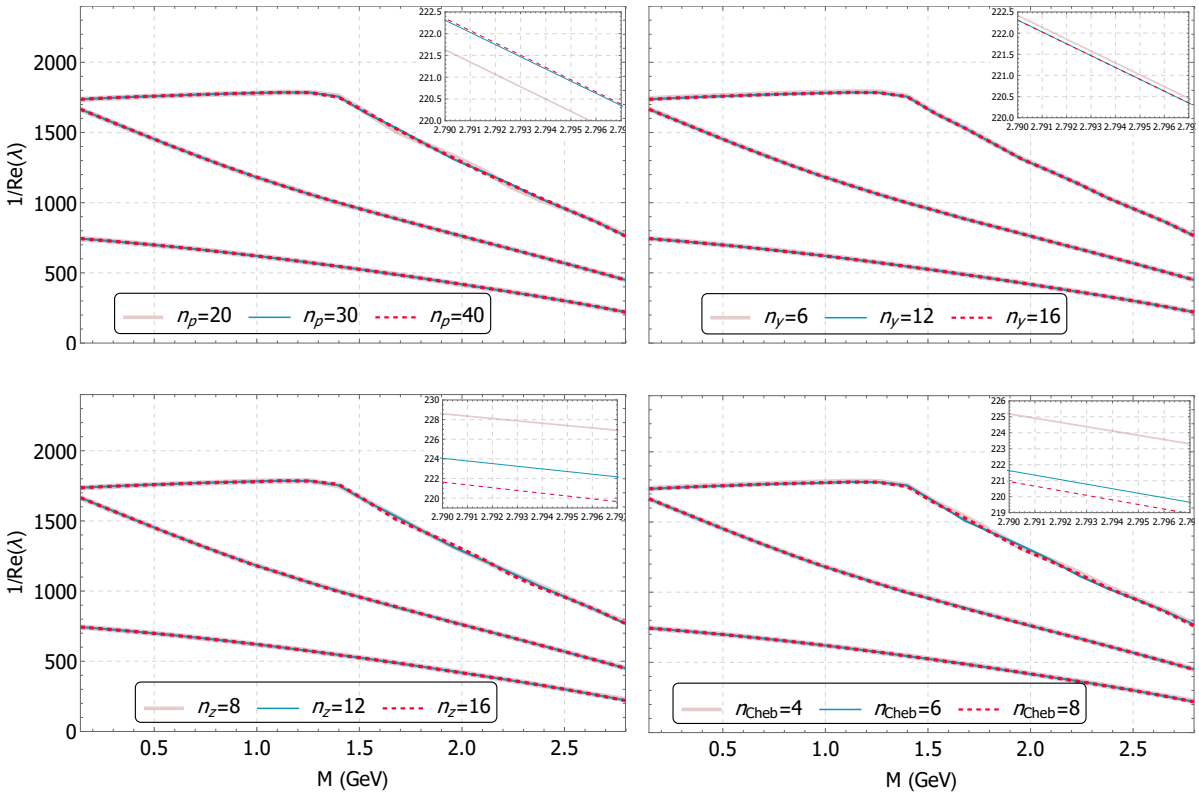

Figure 4.8: Inverse eigenvalue spectrum for all channels and exchanged particles depicted in Figure 3.4. We zoom in the threshold region and depicted the first eigenvalue in the inset pictures in all panels. In the left panels is represented the spectrum with $n_p = 20, n_p = 30$ and $n_p = 40$ (fixing $n_z = 16$, $n_y = 12$ and $n_{Cheb} = 6$) (*top*) and with $n_z = 8, n_z = 12$ and $n_z = 16$ (fixing $n_p = 30$, $n_y = 12$ and $n_{Cheb} = 6$) (*bottom*). In the right panels is presented the spectrum with $n_y = 6, n_y = 12$ and $n_y = 16$ (fixing $n_p = 30, n_z = 16$ and $n_{Cheb} = 6$) (*top*) and with $n_{Cheb} = 4, n_{Cheb} = 6$ and $n_{Cheb} = 8$ (fixing $n_p = 30, n_z = 16$ and $n_y = 12$) (*bottom*).

4.5 Eigenvalues' extrapolation

To reach the physical threshold, which corresponds to the total mass of the constituent particles in the molecule, one has to determine the optimal momentum partitioning, which allows calculations up to that limit. The procedure to determine this parameter is described in Appendix A. Only when the optimal partitioning is employed, the "calculable threshold" corresponds to the physical threshold.

It is straightforward to establish this parameter for the one-channel case, where it is simply given by the mass of the baryon divided by the physical threshold of the molecule. Nevertheless, when there are several channels, we have to define an optimal partitioning for each channel. In our simple model, we stick with the lower threshold, which ensures that we avoid poles; thus our thresholds correspond to the sum of the masses of the lightest baryon and meson in the channels considered. For instance, when we consider all diagrams, the calculable threshold is 2.8 GeV, which coincides with the sum of the lightest baryon, proton, and the lightest meson, $\overline{D}$.

Above the threshold, one has to extrapolate the eigenvalue spectrum which is problematic for several reasons. As a simple "guesstimate", we approximate the p^2-dependence of the eigenvalues by a Hermite polynomial of degree 2. Naturally, the extrapolation is only an indication of each diagram's influence and density of eigenvalues near the threshold region. The inaccuracy of this approach is due to the fact we are continuing a non-analytical function by an analytical since there is a cut opening at the threshold(s). A proper but more involved method to extrapolate the eigenvalues is described in [56].

Chapter 5

Coupling constants

In order to calculate the coupling constants, we need the QCD building blocks, namely the dressed quark propagators, the BS amplitudes, and the dressed vertices. In the case of mesons, the coupling of an external current to a hadron leads to triangle diagrams, which define the impulse approximation plus diagrams where the current couples to the kernel. The triangle diagrams are equivalent to connecting the hadrons by quark propagators.

A possible way to determine the coupling constants is to extract them as residues of the poles in hadronic current matrix elements, and thus as the residues of the form factors that parametrize these matrix elements. We briefly describe method in this chapter.

5.1 Current matrix elements

The form factors are defined as the Lorentz-invariant, Q^2-dependent coefficients in a tensor decomposition of the respective current matrix elements. Like the n-point correlation functions can be expanded into Lorentz invariants and Dirac basis elements, the current-matrix elements can also be expanded [45]. A current matrix element is defined as:

$$\mathcal{J}^{[\mu]}_{\lambda\lambda'}\left(p_f, p_i\right) = \langle\, \lambda\left(p_f\right) \,|\, j^{[\mu]}(0) \,|\, \lambda'(p_i) \,\rangle\,, \tag{5.1}$$

where $\langle\lambda\left(p_f\right)|$ is the outgoing hadron and $|\lambda'(p_i)\rangle$ is the incoming hadron state, and $j^{[\mu]}(z)$ is the current, which is written as

$$j^{[\mu]}(z) = \overline{\psi}(z)\,\Gamma^{[\mu]}\,\psi(z) \quad \Rightarrow \quad \Gamma^{[\mu]} \in \left\{\gamma^\mu, \gamma_5\gamma^\mu, \gamma_5, \dots\right\}, \tag{5.2}$$

where the index $[\mu]$ distinguishes between a vector, axial-vector and pseudoscalar current, respectively.

The current matrix elements themselves are the residues of the poles associated with λ and λ' in elementary Green functions. In the case of mesons and baryons, these are the four- and six-point Green functions, respectively. For the baryon case, the Green functions inserting an external current is

$$G^{[\mu]}_{\alpha\beta\gamma,\tau\sigma\nu}(x_1,x_2,x_3;\,y_1,y_2,y_3,z) := \langle 0|\,\mathsf{T}\,\psi_\alpha(x_1)\psi_\beta(x_2)\psi_\gamma(x_3)\,\overline{\psi}_\tau(y_1)\overline{\psi}_\sigma(y_2)\overline{\psi}_\nu(y_3)\,j^{[\mu]}(z)\,|0\rangle\,, \tag{5.3}$$

where x_i are the positions of the three incoming quarks, and y_i are the positions of the three outgoing particles, and z is the external current's position.

Inserting the completeness relation $I = \sum_\lambda \frac{1}{(2\pi)^3}\int \frac{d^3p}{2E_p}|\lambda\rangle\langle\lambda|$ in eq. (5.3), ensuring that each hadron is on its mass shell ($p^2 = m_\lambda^2$ and $E_p^2 = \vec{p}^{\,2}+m_\lambda^2$) and recalling $\Psi^\lambda_{\alpha\beta\gamma}(x_1,x_2,P) = \langle 0|\,\mathsf{T}\,\psi_\alpha(x_1)\psi_\beta(x_2)\psi_\gamma(x_3)\,|\lambda\rangle$, leads to the seven-point function in momentum space:

$$G^{[\mu]}_{\alpha\beta\gamma,\tau\sigma\nu}(k_f,q_f,p_f;k_i,q_i,p_i) \simeq \sum_{\lambda\lambda'} \frac{\Psi^\lambda_{\alpha\beta\gamma}(k_f,q_f,p_f)}{p_f^2+m_\lambda^2}\,\mathcal{J}^{[\mu]}_{\lambda\lambda'}(p_f,p_i)\,\frac{\overline{\Psi}^{\lambda'}_{\tau\sigma\nu}(k_i,q_i,p_i)}{p_i^2+m_{\lambda'}^2}\,, \tag{5.4}$$

where k and q stands for the relative momenta and p for the total momentum. Thus, one sees that the residue at the mass pole is given by the current matrix element $\mathcal{J}^{[\mu]}$ and the BS wave function Ψ. The equation (5.4) is represented in Figure 5.1 - *left*.

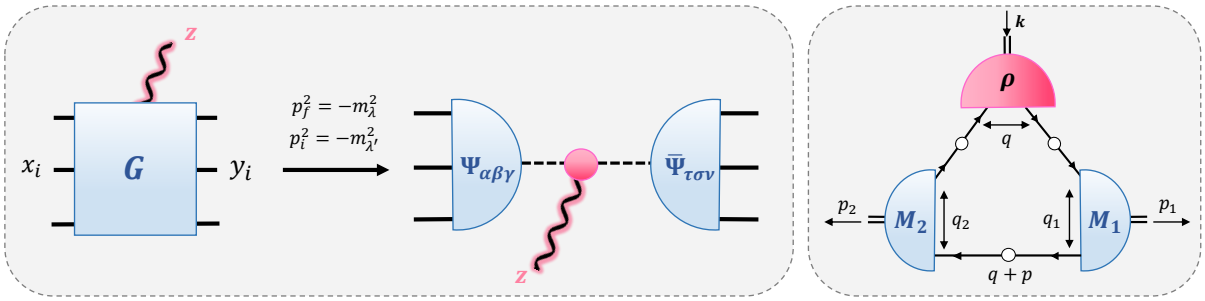

Figure 5.1: Representation of the Green function for the coupling of a current to a baryon and its pole behaviour. The half-circles are the baryons' Bethe-Salpeter wave functions, the dashed line is the Feynman propagator, and the residue at the pole position defines the current matrix element (*left*). In the impulse approximation, the coupling from an external current to mesons is given by triangle diagrams connected by quark propagators (*right*).

As previously mentioned, $G^{[\mu]}$ is obtained from the Green functions G by inserting an external current $j^{[\mu]}(z)$. The current couples linearly to all diagrams in G, thereby one can write:

$$G^{[\mu]} = -G\,(G^{-1})^{[\mu]}\,G \xrightarrow[p_i^2=-m_i^2]{p_f^2=-m_f^2} -\frac{\Psi\,\overline{\Psi}(k_f,q_f,p_f)}{p_f^2+m_f^2}\,(G^{-1})^{[\mu]}\,\frac{\Psi\,\overline{\Psi}(k_i,q_i,p_i)}{p_i^2+m_i^2}\,, \tag{5.5}$$

where we used the definition of G, given in eq. (2.26), and the momenta dependence on G was omitted for simplicity.

Comparing eqs. (5.4) and (5.5), one can derive the expression for the current matrix element, which is written as:

$$\mathcal{J}^{[\mu]}(p_f,p_i) = -\overline{\Psi}(k_f,q_f,p_f)\,(G^{-1})^{[\mu]}\,\Psi(k_i,q_i,p_i)\,. \tag{5.6}$$

Thus, in principle, we could extract form factors by isolating the pole behavior in the original n-point function (given in eq. (5.3)). However, this is not necessary since we derived an expression for the current matrix element $\mathcal{J}^{[\mu]}$ directly, from the dressed quark propagators, vertices and Bethe-Salpeter amplitudes.

5.2 Hadronic decays

In practice, to compute these matrix elements one needs solutions for several integral equations, in particular, the quark DSE (given in eq. (2.2)), the meson and diquark BSEs, and, in the context of baryons, the three-quark (or quark-diquark) BSE.

The vector, scalar or pseudoscalar structure of the form factors is entirely carried by the respective vertices, which have several model-independent consequences for the form factors, including timelike meson poles, where the coupling constants are calculated.

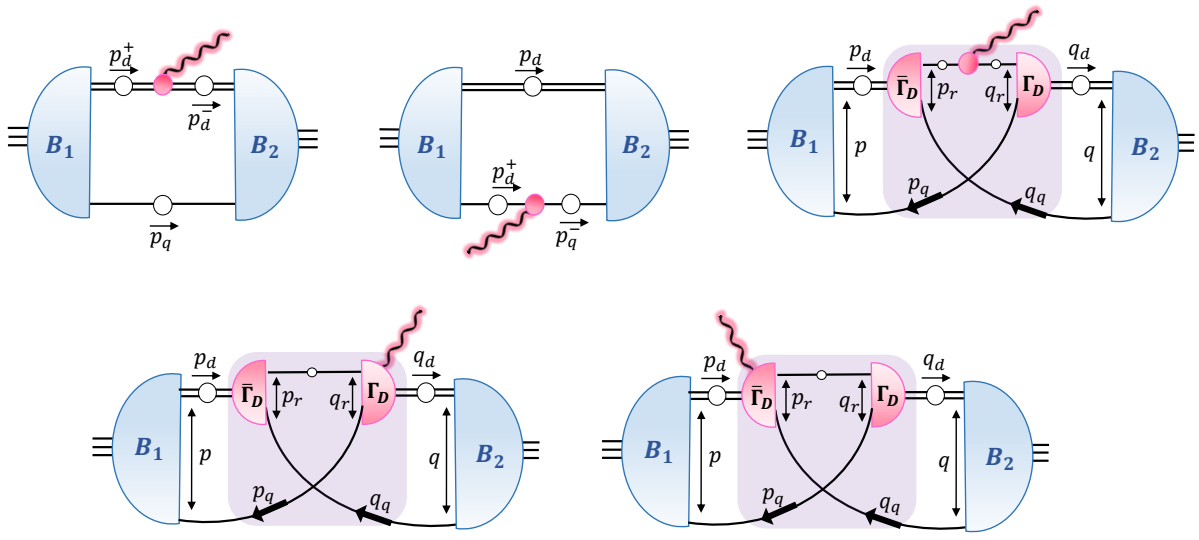

Figure 5.2: Representation of the coupling of an external current to a baryon in the quark-diquark picture. The coupling is given by the sum of the couplings to the diquark (*top* - *left*), the quark (*top* - *middle*), quark-diquark kernel (*top* - *right*) and to the diquark amplitudes - seagull diagrams (*bottom*).

5.2.1 Building blocks

In the impulsive approximation, the hadronic BS amplitudes are connected by quark propagators, as represented in Fig. 5.1 - *right*. In addition, we consider the rainbow-ladder truncation, which substitutes the fully dressed quark-gluon vertex with a bare vertex. Its counterpart in a hadronic bound-state equation is a gluon ladder kernel, this is a dressed iterated gluon exchange between two quarks (see [45, 49] and references therein). The meson amplitude is written as

$$\Gamma_M(p,P) = -\frac{4}{3}\int_q \mathcal{G}(k^2)\frac{T_k^{\mu\nu}}{k^2}\gamma^\mu \chi_M(q,P)\gamma^\nu\,, \tag{5.7}$$

where the factor $4/3$ is the color trace, $\mathcal{G}(k^2)$ is an effective interaction model, and $\chi(q,P) = S(q_+)\,\Gamma(q,P)\,S(q_-)$ is the BS wave function.

The diquarks are in many respects conceptually similar to mesons. The diquark correlations appear as structures in a quark-quark system whose properties can depend on the truncation or the effective interaction. RL produces timelike diquark poles, although this could be a truncation effect and disappear beyond the RL truncation. The resulting diquark BSE reads

$$\Gamma_D(p,P)\,C = -\frac{2}{3}\int_q \mathcal{G}(k^2)\frac{T_k^{\mu\nu}}{k^2}\gamma^\mu \chi_D(q,P)\,C\,\gamma^\nu\,, \tag{5.8}$$

where C is the charge conjugation, and $\chi_D(q,P)$ is the diquark wave function defined as $\chi_D(q,P)\,C = S(q_+)\,\Gamma(q,P)_D\,C\,S(q_-)$.

Baryons can be interpreted as a quark-diquark systems bound by an iterative quark exchange, in which case the amplitude is given by:

$$\Gamma_B^\alpha(p,P) = c^{(\alpha\beta)}\int_k K^{\alpha\beta}_{Q-DQ}\,S(k_q)\,D^{\beta\beta'}(k_d)\,\Gamma_B^{\beta'}(k,P)\,, \tag{5.9}$$

where $c^{(\alpha\beta)}$ is the color-flavor trace, $D^{\beta\beta'}$ represents the diquark propagator, and $K^{\alpha\beta}_{Q-DQ} = \Gamma^\beta_D(k_r,k_d)\,S^T(q)\,\overline{\Gamma}^\alpha_D(p_r,p_d)$ is the quark-diquark kernel. The coupling of an external current to a baryon is represented in Fig. 5.2.

5.2.2 Vertices and form factors

With all ingredients calculated beforehand, one determines the current-matrix elements. Let us consider the triangle diagram depicted in Fig. 5.1. In this case, a vector particle (ρ) couples to mesons M_1 and M_2. The current matrix element is calculated from the previous ingredients and reads

$$\mathcal{J}^\mu_{\rho M_1 M_2}(p,k) = \mathrm{Tr}\int_q \overline{\Gamma}_{M_2}(q_2,p_2)\,S(q+p)\,\overline{\Gamma}_{M_1}(q_1,p_1)\,\chi^\mu_\rho(q,k)\,, \tag{5.10}$$

where k is the momentum of the vector particle, and $\overline{\Gamma}$ is the charge conjugated on-shell meson amplitude, calculated from its BSE (eq. (5.7)). $S(q+p)$ is the renormalized dressed quark propagator obtained from its DSE (eq. (2.2)), and $\chi^\mu_\rho(q,k)$ is the vector wave function. All mesons are on-shell.

The most general Dirac-Lorentz structure of the amplitude can be parameterized as:

$$\mathcal{J}^\mu_{\rho M_1 M_2}(p,k) = 2\,g_{\rho M_1 M_2}\,p^\mu\,, \tag{5.11}$$

where $g_{\rho M_1 M_2}$ is the coupling constant and p^μ is the relative momentum between the two pseudoscalar mesons. This corresponds to the most general tensor structure of a pseudoscalar-pseudoscalar-vector vertex, as depicted in Figure 3.2. Comparing equations (5.10) and (5.11) is possible to calculate the form factor/coupling constant.

For the remaining meson vertices, we could employ the same method. After calculating the current-matrix element, we compare the result with the most general Lorentz invariant structure (given in Figure 3.2).

In the baryon case, one starts by identifying the current of the three quark T-matrix on the baryon mass shell. The hadronic matrix elements of the current are obtained by the sum of diagrams that describe the coupling of the current to all ingredients at the constituent level. In the case of a quark-diquark baryon, the ingredients are the quark propagator, the diquark propagator and the kernel, as depicted in Figure 5.2. Then, the current matrix element is the sum of these contributions.

Chapter 6

Results

The main result of this thesis is the determination of the eigenvalue spectrum and masses of the bound states in the meson-baryon system obtained with one-boson exchanges. In order to do that, we calculate the eigenvalues of the system and determine the value of P^2 where the inverse eigenvalues cross the coupling constant's value. Also, we plot the eigenvectors, which are the components of the Bethe-Salpeter amplitudes, to analyze the behavior of each basis element.

Finally, we identify the relevant channels to describe the pentaquark states discovered at LHC, by comparing the mass spectra.

6.1 Eigenvalue spectrum

First, we consider only one channel (see Figure 3.4), the $\Sigma_c\{\overline{D}, \overline{D}^*\} \leftrightarrow \Sigma_c\{\overline{D}, \overline{D}^*\}$. The configurations studied for this channel are given in Figure 6.7. The second channel is then added, the $J/\psi p \leftrightarrow \eta_c p$, to check the eigenvalue spectrum response. The cases, including the second channel, are indicated in Figure 6.8. Eigenvalues comparison will allow for the assessment of their influence in the pentaquark system and determine how each channel and exchange particles affect the number of bound states. The masses of these particles are given in Table B.1. The inverse eigenvalues are calculated up to the accessible threshold (see Appendix A) and extrapolated by a Hermite polynomial above it (as described in section 4.5).

6.1.1 $\mathbf{\Sigma_c\{\overline{D}, \overline{D}^*\} \leftrightarrow \Sigma_c\{\overline{D}, \overline{D}^*\}}$ channel

We begin by adding diagrams to the first channel $\Sigma_c\{\overline{D}, \overline{D}^*\} \leftrightarrow \Sigma_c\{\overline{D}, \overline{D}^*\}$, as indicated by configurations **(C1) - (C6)** in Figure 6.7. The eigenvalue spectrum for different combinations is depicted in Figure 6.1.

In Figure 6.1 - **(C1)** and **(C2)**, we plot the inverse eigenvalue spectrum for the diagonal diagrams, individually, and looking at these configurations in Figure 6.7, we expect these diagrams to be decoupled, since they belong to the diagonal part of the kernel matrix. Hence, comparing the inverse eigenvalue spectrum of **(C1)** and **(C2)** with configuration **(C3)**, which includes both diagonals, we conclude that the

ground and first excited state in **(C3)** are identified as the ground state in **(C1)** and the ground state in **(C2)**, respectively. The second and third excited states in **(C3)** have contributions from both diagrams. In particular, the second excited state is given by the first excited state in **(C2)** until around M=1 GeV and after that by the first excited state in **(C1)**. Regarding the third excited state, it is the other way around, it is dominated by the second excited state from **(C2)** until M=1 GeV and then by **(C1)**. Because the spectrum in **(C3)** can be approximately obtained by superimposing spectra **(C1)** and **(C2)**, from which one can conclude that these two diagrams are essentially decoupled.

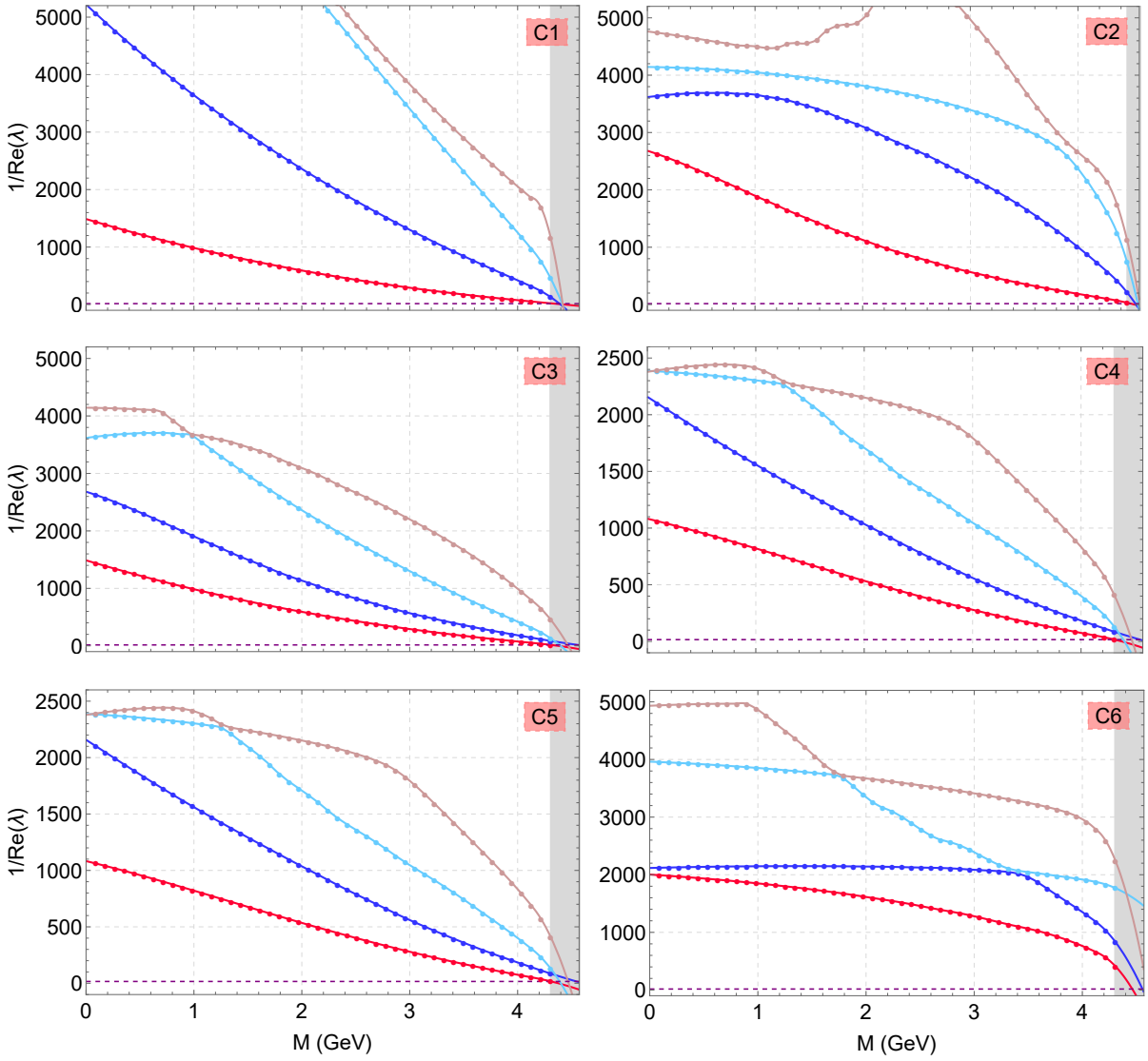

Figure 6.1: Inverse eigenvalue spectrum for the configurations **(C1) - (C6)** in Figure 6.7 considered for the 1^{st} channel. The gray area represents the region above the threshold where the eigenvalues are extrapolated. The dots are the calculated values, the lines are inter- and extrapolation.

Afterwards, the off-diagonal diagrams **(C4)** are included. From the inverse eigenvalue spectrum comparison with **(C3)**, we observe that the they are similar, but the inverse eigenvalues' magnitude in

(C4) is lower, indicating that the off-diagonal diagrams have an attractive effect in the system; however they are not dominant. Next, we depict the inverse eigenvalue spectrum for **(C5)**, and by comparing with **(C4)**, we observe that the spectra are very close to each other, meaning that the ρ exchange in the off-diagonal diagrams is responsible for more binding in the full channel configuration, **(C4)**, and the π exchange could be neglected in this channel. For completeness, we present the off-diagonal diagrams, only **(C6)**, but as previously mentioned, these diagrams are subdominant. Thus, we conclude that by themselves they fail in reproducing the spectrum for this channel. The magnitude of these inverse eigenvalues is comparable to other configurations; however this might be an artifact of our model, as we employed the same coupling constant for all diagrams, but in reality the off-diagonals may have a smaller coupling strength and become even more negligible.

To summarize, the first channel is essentially dominated by the diagonal diagrams, namely, in the ground state the $\Sigma_c\overline{D} - \Sigma_c\overline{D}$ diagram prevails, the first excited state is dominated by $\Sigma_c\overline{D}^* - \Sigma_c\overline{D}^*$ and the higher lying inverse eigenvalues are given by contributions from both diagonal diagrams. From now on, configuration **(C4)** will be taken as our reference.

6.1.2 $\mathbf{\Sigma_c\{\overline{D}, \overline{D}^*\} \leftrightarrow \Sigma_c\{\overline{D}, \overline{D}^*\}}$ and $\mathbf{p\{\eta_c, J/\psi\} \leftrightarrow p\{\eta_c, J/\psi\}}$ channels

Beyond the 1^{st} channel, we add the 2^{nd} according to configurations **(C7) - (C12)** in Figure 6.8, and represent the inverse eigenvalue spectrum in Figure 6.2.

We plot the inverse eigenvalue spectrum for **(C7)**, and comparing with our reference **(C4)** (represented by the dashed lines in all panels), one concludes that it merely shifts the spectrum. In addition, we only consider the vector-vector diagonal diagram **(C8)**, and the spectrum is almost identical to **(C7)**, but in this case the ground state is very close to our reference, meaning that the small shift from the diagonal diagrams comes from $\Sigma_c D \leftrightarrow p\,\eta_c$. Subsequently, we plot **(C9) - (C11)**, and they all look similar even in form and magnitude, indicating that there is not a particular off-diagonal diagram which is dominant. Also, the ground state is almost not changed by any of these configurations.

Finally, we represent **(C12)**, which includes all diagrams, and by comparing with **(C4)** we observe, once more, that the spectrum looks very similar. The main difference is on the inverse eigenvalue spectrum magnitude which is lowered by the interference from the diagonal and off-diagonal diagrams of the 2^{nd} channel, since individual configurations **(C7)-(C11)** fail themselves in explaining the spectrum **(C12)**. Despite the second channel having an attractive effect, providing more binding, it does not modify the eigenvalues fundamentally. Thus, the system is still dominated by the first channel, mainly by the diagonal diagrams.

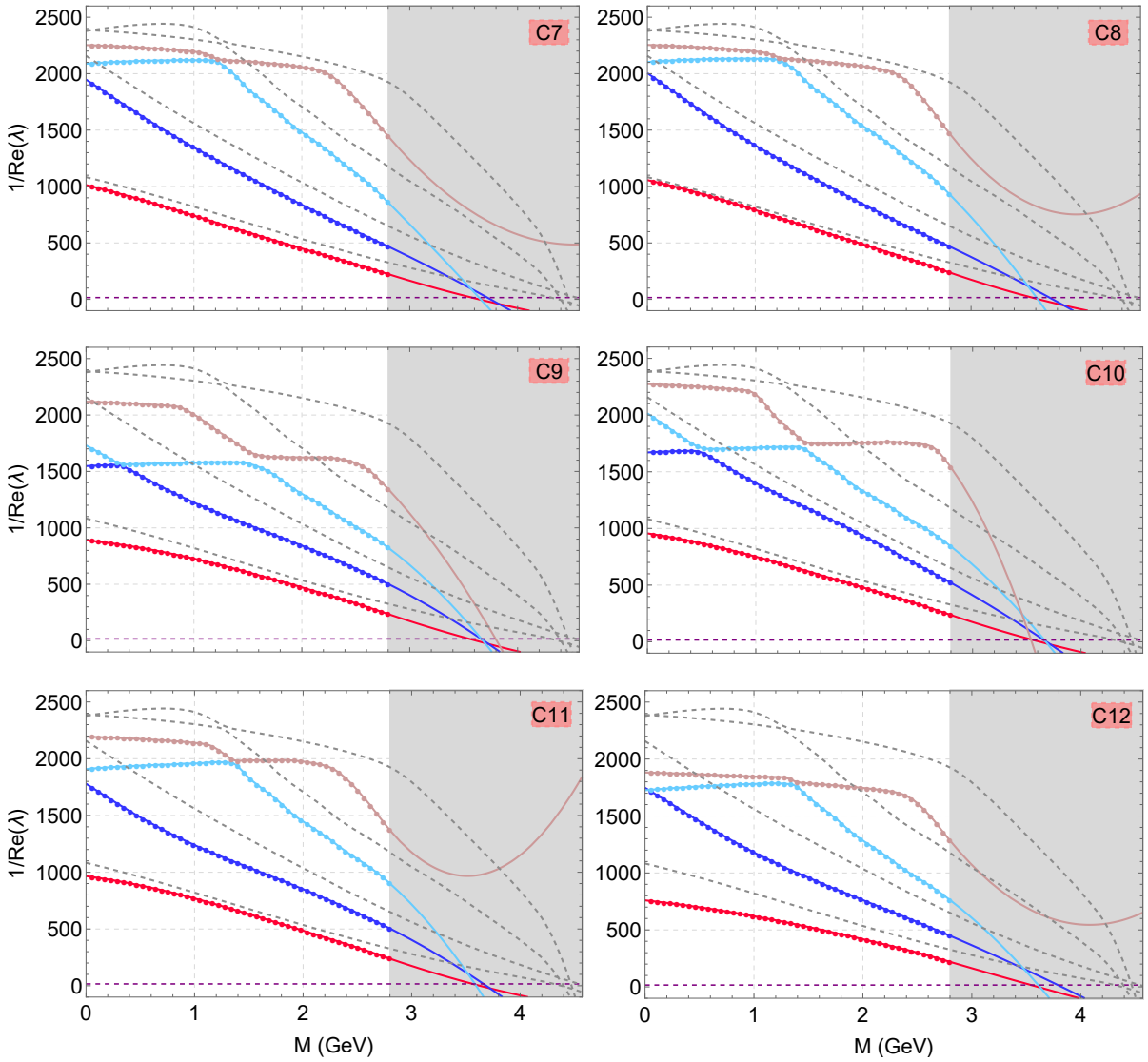

Figure 6.2: Inverse eigenvalue spectrum for configurations **(C7) - (C12)** in Figure 6.7 considered for the 1^{st} and 2^{nd} channel. The gray area represents the region above the threshold. The dashed gray lines are the results of the reference configurations **(C4)**, shown for comparison.

6.2 Mass spectra

In this section, we present the mass spectra for some cases considered in the previous subsections 6.1.1 and 6.1.2. The masses of the bound states $P^2 = -M^2$ are obtained by the intersection of the inverse eigenvalues with the coupling constant value. In our case, the coupling constant is chosen such that the ground state reproduces the mass of the lightest pentaquark state detected at LHC, the $P_c(4312)^+$, in our reference calculation **(C4)**. This value was found to be $c = 16.0$, which is employed in the other configurations to determine the density of bound states. As previously mentioned, this is simply a first approximation, since, in principle, one could calculate the coupling constants as described in Chapter 5. The masses determined in this section are merely a rough indication, whenever they are calculated above the threshold. An evidence of the fragility of Hermite extrapolation is the occurrence of eigenvalue

crossing, which should not happen after the reconstruction procedure. We calculate the extrapolation until 4.457 GeV, which corresponds to the pentaquark state with the largest mass, $P_c(4457)^+$. We only consider the first three inverse eigenvalues as an illustration. Also, higher magnitude inverse eigenvalues are associated with larger uncertainties.

6.2.1 $\Sigma_c\{\overline{D}, \overline{D}^*\} \leftrightarrow \Sigma_c\{\overline{D}, \overline{D}^*\}$ channel

In Figure 6.3, the purple horizontal line is adjusted such that the first bound state in **(C4)** is at 4.312 GeV. As previously determined, the ground state in configuration **(C1)** gives the ground state in **(C4)**, the mass of that state is the same in both cases (M = 4.312 GeV). While in the first excited state prevails the contribution from the ground state in **(C2)**, thus the mass of the next bound state in **(C4)** should appear near 4.492 GeV. However, the second excited state in **(C4)** forms a bound state before the first excited state, as a consequence of our oversimplified extrapolation. So, if we overlook this "problematic" state, the first excited state in **(C4)** forms a bound state near 4.545 GeV. The bound states of **(C5)** are basically the same as in our reference **(C4)**, as anticipated by the inverse eigenvalue spectrum analyses in 6.1.1.

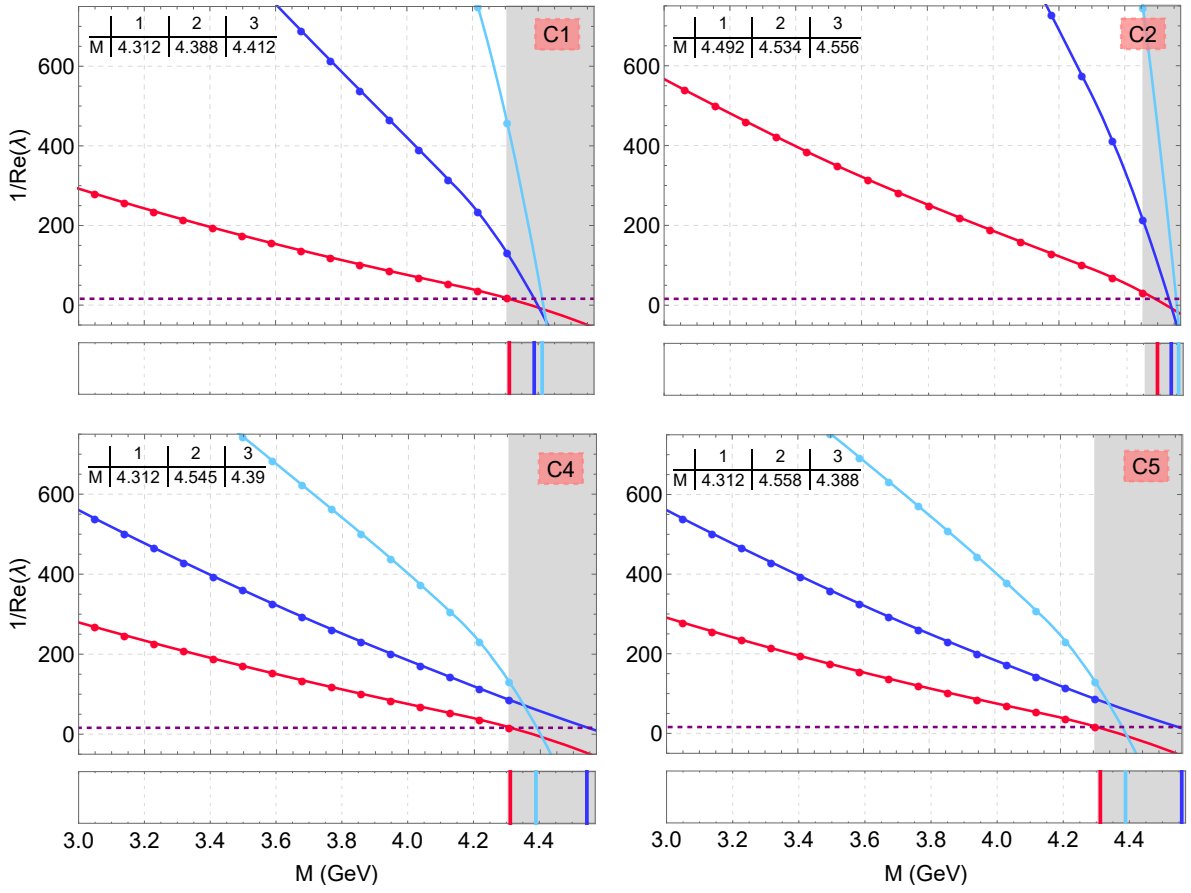

Figure 6.3: Inverse eigenvalue spectrum near the threshold and bound state masses for configurations **(C1), (C2), (C4)** and **(C5)**. The horizontal line corresponds to the adjusted coupling constant value, $c = 16.0$. The gray area represents the region above the threshold, where the inverse eigenvalues are extrapolated. In the inset tables are indicated the bound state masses (in GeV) for the three inverse eigenvalues.

6.2.2 $\Sigma_c\{\overline{D}, \overline{D}^*\} \leftrightarrow \Sigma_c\{\overline{D}, \overline{D}^*\}$ and $p\{\eta_c, J/\psi\} \leftrightarrow p\{\eta_c, J/\psi\}$ channels

In Figure 6.4, we represent the bound state masses when including the second channel. In this case, it is even more difficult to get the masses of the bound states since we are far below the physical threshold and the region where the inverse eigenvalues are extrapolated is very broad. Nevertheless, we plot them for completeness.

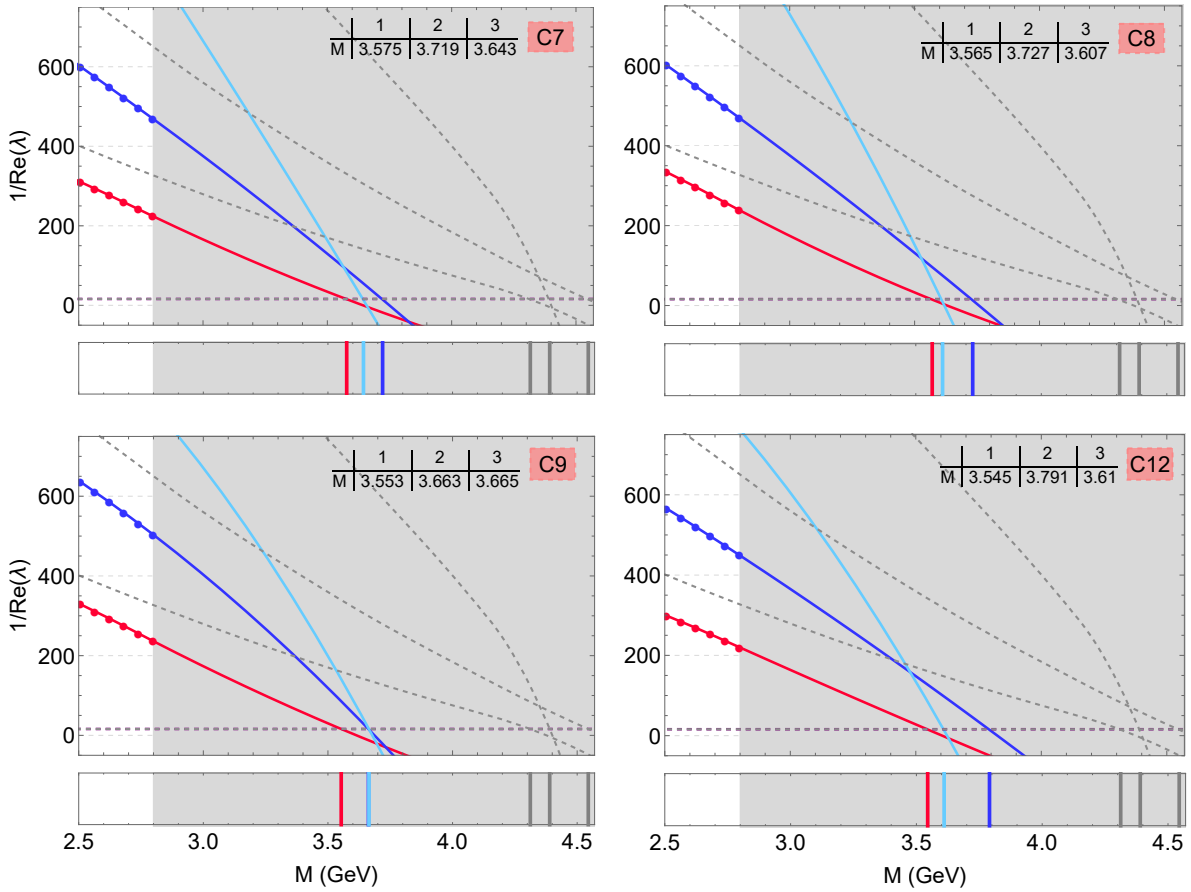

Figure 6.4: Inverse eigenvalue spectrum near the threshold and bound state masses for configurations **(C7), (C8), (C9)** and **(C12)**. The horizontal line corresponds to the adjusted coupling constant value, $c = 16.0$. The gray area represents the region above the threshold, where the inverse eigenvalues are extrapolated. The dashed lines show the eigenvalues of our reference case **(C4)**. In the table is indicated the bound state masses for the three eigenvalues.

The configurations **(C7)** and **(C8)** have a similar inverse eigenvalue spectrum, consequently their bound state masses are close to each other. **(C9)** shows the bound states formed by the off-diagonal diagrams. Comparing **(C7)**, **(C8)** and **(C9)**, the bound state masses created by the ground states are quite close (M = 3.575, 3.565, 3.553 GeV), as expected by their eigenvalues spectrum analyses in section 6.1.2. If we overlook the inverse eigenvalue crossing due to the second excited state, the masses created by the first excited states are similar **(C7)** and **(C8)** (M = 3.719, 3.727 GeV). We represent the complete configuration **(C12)**, and observe that the ground state is still close to the other configurations

(M = 3.545 GeV), thus they are not affected by any particular diagram in the 2^{nd} channel. The bound state mass created by the first excited state (M = 3.791 GeV) is not as close as the ones produced by the same eigenvalue in the diagonal diagrams **(C7)** (M = 3.719 GeV) and **(C8)** (M = 3.727 GeV), given that higher eigenvalues have larger uncertainties. We have to highlight that the masses are much lower than in the 1^{st} channel due to the inverse eigenvalues shift, probably as a result of the extrapolation, but the fact that the bound state distribution is close to each other in **(C7)**, **(C8)** and **(C9)** is evidence that the system is not much altered by any particular diagram in the 2^{nd} channel.

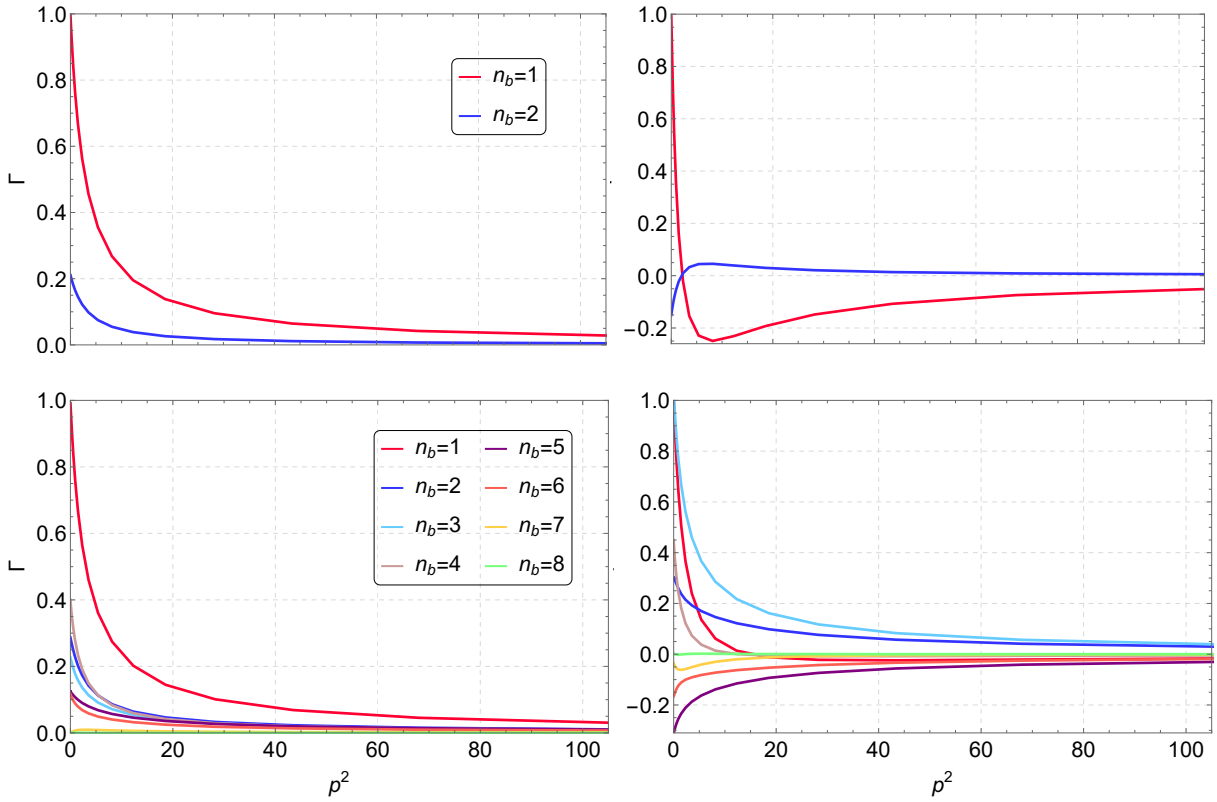

Figure 6.5: Bethe-Salpeter amplitudes for configurations **(C1)** (*top*) and **(C4)** (*bottom*). The ground state amplitudes are represented on the left panels and the first excited states on the right. In all cases, we selected $m_{Cheb} = 0$. The amplitudes are relatively normalized with respect to the largest amplitude at $p^2 = 0$ in each case.

6.3 Bethe-Salpeter amplitudes

In this section, we plot the eigenvectors that correspond to the Bethe-Salpeter amplitudes of configurations **(C1)** and **(C4)**. These cases are depicted as an illustration of the behavior of the amplitude. In principle, performing an accurate analysis of the BSAs allows drawing conclusions about the structure of the states. Also, comparing their shape and magnitude for different diagrams provides a quantitative analysis of the structure encoded in each configuration. However, this study would require a proper calculation of the coupling constants as well as an absolute normalization of the amplitudes, which was not done in our study. We normalized them relatively, by the largest amplitude at $p^2 = 0$ in each case.

Figure 6.5 shows the BSAs for configurations **(C1)** and **(C4)** for the ground and first excited state, where one can observe that they have the correct fall-off behavior for large p^2 values.

In the particular case of amplitudes with $n_b = 1, 2$ for the ground states in **(C1)** and **(C4)**, it is straightforward to compare them and observe that they are similar, as depicted in Figure 6.6. This similarity corroborates and complements our previous conclusions about the dominance of $\Sigma_c\overline{D} - \Sigma_c\overline{D}$ in the ground state of the first channel, meaning that this diagram represents indeed the leading contribution to the channel as well as the structure of the state. Also, other diagrams in the first channel do not change the structure of the scalar amplitudes.

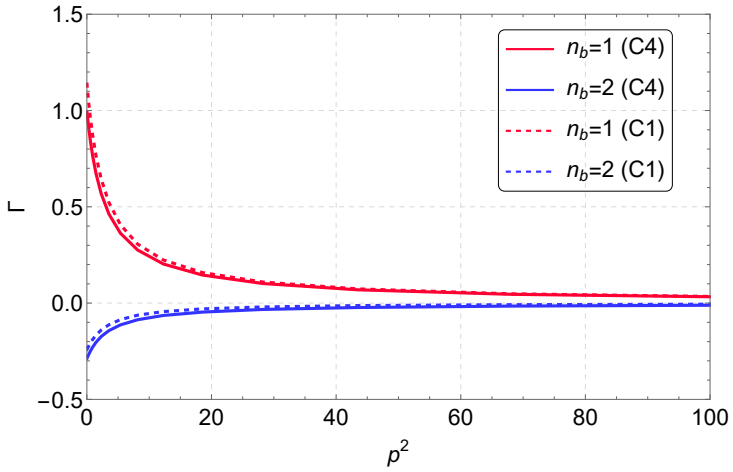

Figure 6.6: Comparison between the scalar BSAs for configurations **(C1)** and **(C4)**. In this case, the amplitudes are normalized to $n_b = 1$ in **(C4)**.

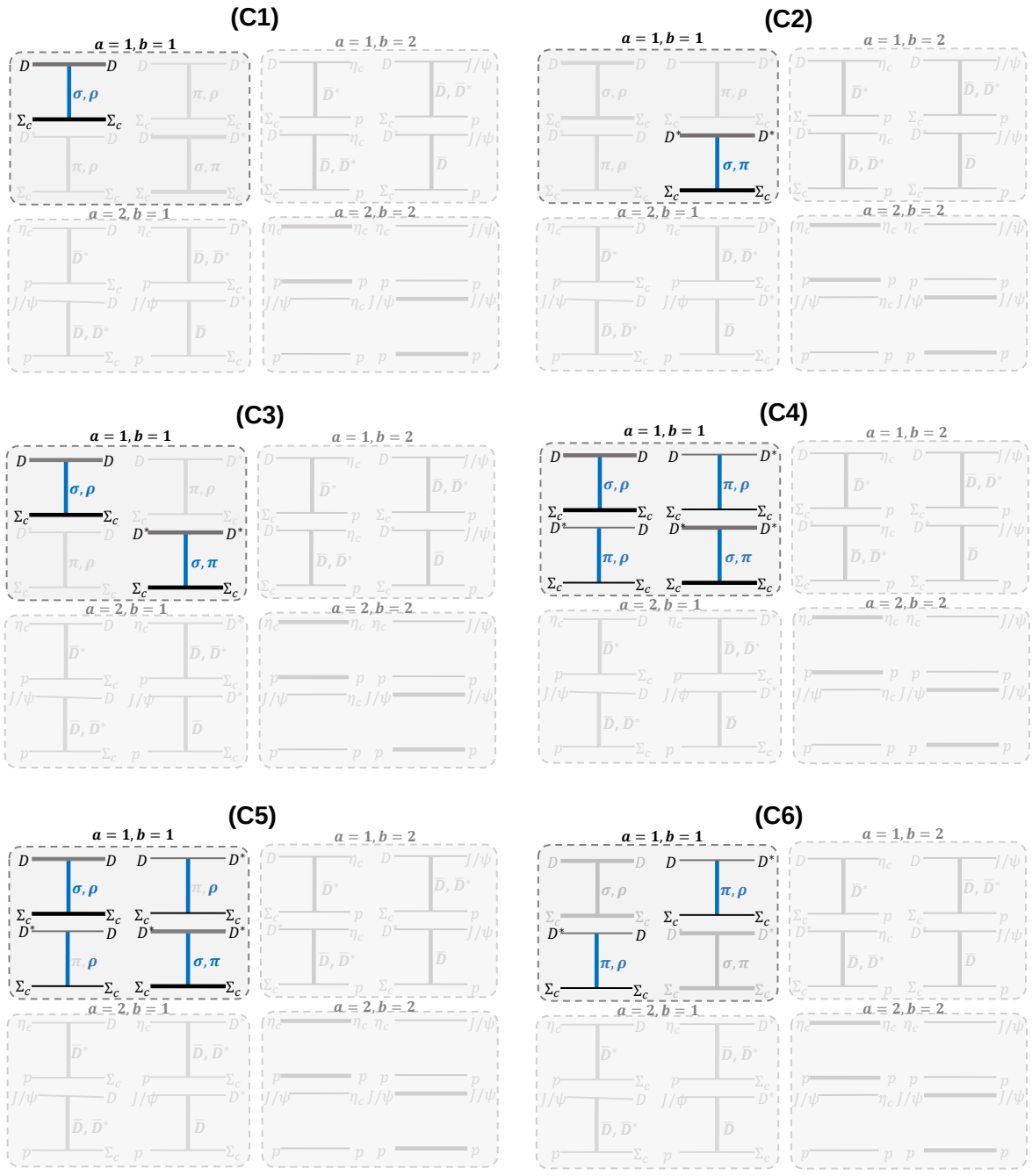

Figure 6.7: Different configurations considered for the first channel.

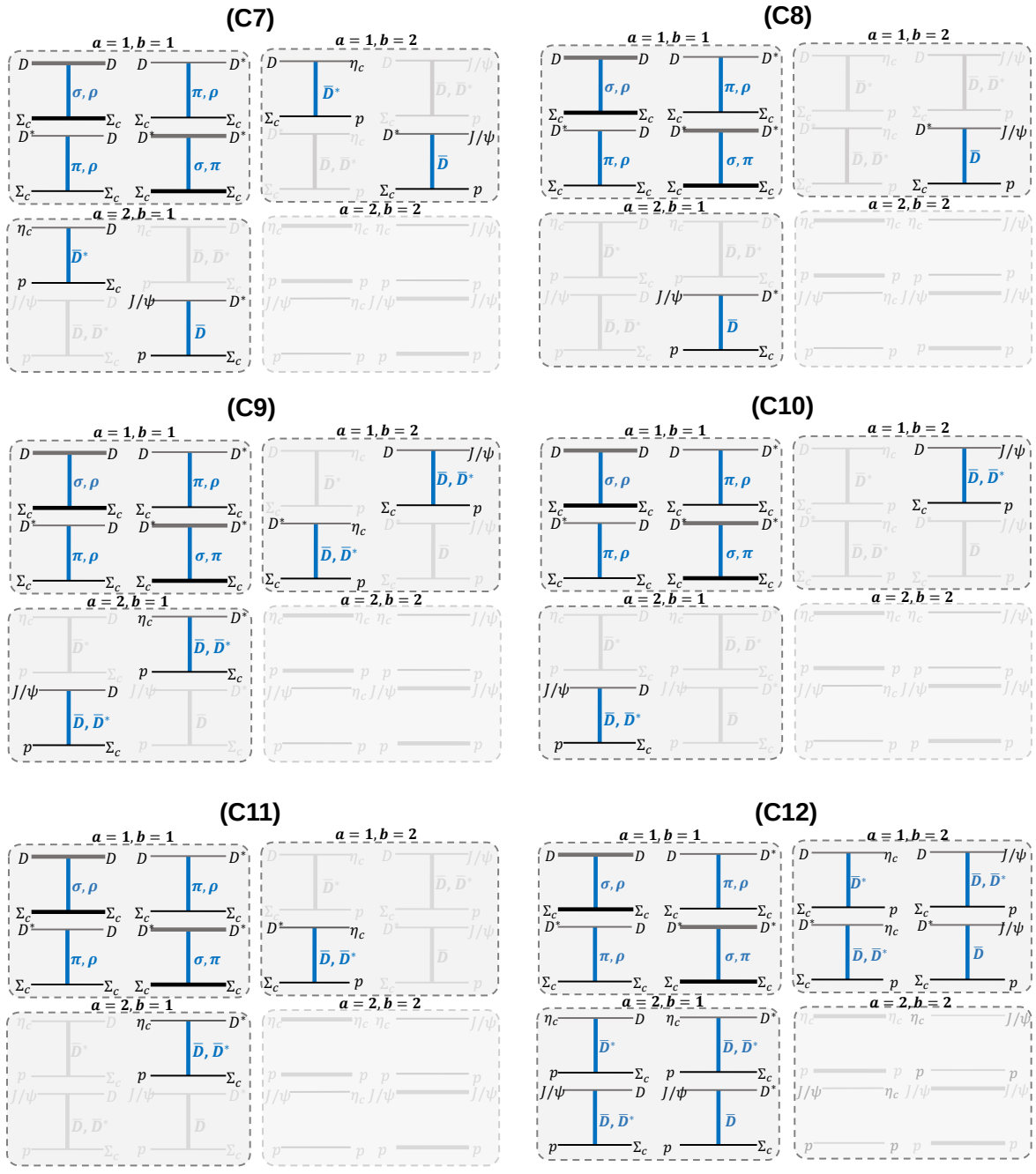

Figure 6.8: Different configurations considered after adding the second channel.

Chapter 7

Concluding remarks and further work

7.1 Conclusions

The goal of this thesis project was to calculate pentaquark states in QCD within the Bethe-Salpeter formalism. The main objective was to make predictions about the dominant diagrams to describe these states and their bound state masses. In our calculations, we assumed a molecular picture, constituted by a meson and a baryon suitable to form the appropriate quark content, $\bar{c}cuud$. Hadronic exchanges bind the molecule.

In order to draw conclusions, we plotted the inverse eigenvalue spectrum for different configurations, including the two possible channels, the $\Sigma_c\{\overline{D}, \overline{D}^*\} \leftrightarrow \Sigma_c\{\overline{D}, \overline{D}^*\}$ and the $p\{\eta_c, J/\psi\} \leftrightarrow p\{\eta_c, J/\psi\}$. Then, by comparing each channel's influence in the spectrum, we concluded that the second channel does not affect it fundamentally. It only decreases the inverse eigenvalues by providing more binding to the system. Thus, the pentaquark could be generally described by the first channel alone, as long as the molecules $\Sigma_c\overline{D}$ and $\Sigma_c\overline{D}^*$ are included. Inside the first channel, the diagonal diagrams are the most relevant to describe the system, so the case where both diagrams are included was taken as our reference case.

Afterwards, we calculated the bound state masses formed for the several combinations by fixing the coupling constant such that the first bound state in our reference case appears at the mass of the lightest pentaquark discovered at LHCb, $P_c(4312)^+$. This value was found to be $c = 16.0$. In our reference case, for the ground and first excited state, we found M = 4.312 and 4.545 GeV, respectively.

Our model is simply a first approximation; all coupling constants were taken to be equal; however, this is not a very realistic model. Each diagram has a specific coupling constant, that could be adequately calculated in future work. Another source of uncertainty is the inverse eigenvalue extrapolation above the threshold, where the masses are calculated. In principle, the predictions in this region can be made through the Resonances-Via-Padé method. Thus, our bound state masses are only an indication of the density of inverse eigenvalues near the threshold region, and should not be taken as a firm prediction.

7.2 Future work

The next step would be to solve the same meson-baryon system, but with the interaction given by a genuine quark exchange instead of a one-boson exchange, which can be derived from the five-body equation for the pentaquark under certain approximations. This system is shown in Figure 3.1 - (*middle*) and depicted with more detail in Figure 7.1.

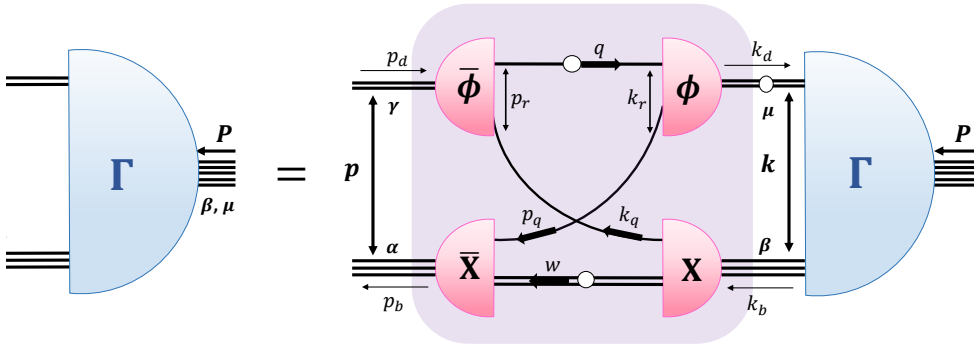

Figure 7.1: Bethe-Salpeter equation for the meson-baryon molecule with quark exchanges.

If all ingredients are calculated consistently from their DSEs and BSEs, this approach has the advantage of having fewer parameters: e.g., in RL the only model input is the effective interaction. The suppression trough the vertex form factors would be an automatic dynamical outcome of these calculations, so it is not necessary to introduce them explicitly.

Bibliography

[1] N. E. Booth, A. Abashian, K. M. Crowe, *Phys. Rev. Lett.* **7**, 35 (1961).

[2] G. Rochester, C. Butler, *Nature* **160**, 855 (1947).

[3] M. Gell-Mann, *Phys. Lett.* **8**, 214 (1964).

[4] G. Zweig, *Developments in the Quark Theory of Hadrons. Volume 1*, D. Lichtenberg, S. P. Rosen, eds. (Hadronic Press, 1964), pp. 22–101.

[5] V. Ginzburg, *Physics and Astrophysics*, V. Ginzburg, ed. (Pergamon, 1985), pp. 36 – 67.

[6] C. Alt, *et al.*, *Phys. Rev. Lett.* **92**, 042003 (2004).

[7] I. Abt, *et al.*, *Phys. Rev. Lett.* **93**, 212003 (2004).

[8] T. Xiao, S. Dobbs, A. Tomaradze, K. Seth, *Phys. Lett. B* **727**, 366 (2013).

[9] R. Aaij, *et al.*, *Phys. Rev. Lett.* **115**, 072001 (2015).

[10] R. Aaij, *et al.*, *Phys. Rev. Lett.* **117**, 082003 (2016).

[11] R. Aaij, *et al.*, *Phys. Rev. Lett.* **122**, 222001 (2019).

[12] R. Aaij, *et al.*, *Science Bulletin* **65**, 1983 (2020).

[13] A. Ali, J. S. Lange, S. Stone, *Prog. Part. Nucl. Phys.* **97**, 123 (2017).

[14] S.-K. Choi, *et al.*, *Phys. Rev. Lett.* **91**, 262001 (2003).

[15] F.-K. Guo, *et al.*, *Rev. Mod. Phys.* **90**, 015004 (2017).

[16] O. Stern, R. Frisch, *Z. Phys.* **85**, 4 (1933).

[17] E. D. Bloom, *et al.*, *Phys. Rev. Lett.* **23**, 930 (1969).

[18] R. H. Dalitz, S. F. Tuan, *Phys. Rev. Lett.* **2**, 425 (1959).

[19] M. Alston, *et al.*, *Phys. Rev. Lett.* **6**, 300 (1961).

[20] H. J. Behrend, *et al.*, *Phys. Rev. Lett.* **15**, 900 (1965).

[21] J. Hall, *et al.*, *Phys. Rev. Lett.* **114**, 132002 (2014).

[22] H. Lipkin, *Phys. Lett. B* **195**, 484 (1987).

[23] M. Gell-Mann, *Phys. Rev.* **125**, 1067 (1962).

[24] Y. Ne'eman, *Nucl. Phys.* **26**, 222 (1961).

[25] M. Y. Han, Y. Nambu, *Phys. Rev.* **139**, B1006 (1965).

[26] H. Fritzsch, M. Gell-Mann, H. Leutwyler, *Phys. Lett. B* **47**, 365 (1973).

[27] H. Fritzsch, *Inter. Jour. Mod. Phys. A* **34**, 1930001 (2019).

[28] H. D. Politzer, *Phys. Rev. Lett.* **30**, 1346 (1973).

[29] D. J. Gross, F. Wilczek, *Phys. Rev. Lett.* **30**, 1343 (1973).

[30] J. Goldstone, *Nuovo Cimento* **19**, 154 (1960).

[31] Z.-C. Yang, Z.-F. Sun, J. He, X. Liu, S.-L. Zhu, *Chin. Phys. C* **36**, 6 (2012).

[32] W. L. Wang, F. Huang, Z. Y. Zhang, B. S. Zou, *Inter. Jou. Mod. Phys.: Conference Series* **26**, 1460071 (2014).

[33] L. Roca, J. Nieves, E. Oset, *Phys. Rev. D* **92**, 094003 (2015).

[34] R. Chen, X. Liu, S.-L. Zhu, *Nuc. Phys A* **954**, 406 (2016).

[35] H. Huang, C. Deng, J. Ping, F. Wang, *Eur. Phys. Jour. C* **76**, 624 (2016).

[36] Y.-H. Lin, B.-S. Zou, *Phys. Rev. D* **100**, 056005 (2019).

[37] R. F. Lebed, *Phys. Lett. B* **749**, 454 (2015).

[38] R. Zhu, C.-F. Qiao, *Phys. Lett. B* **756**, 259 (2016).

[39] Z.-G. Wang, *Eur. Phys. Jour. C* **76**, 70 (2016).

[40] L. Maiani, A. D. Polosa, V. Riquer, *Phys. Lett. B* **749**, 289 (2015).

[41] G.-N. Li, X.-G. He, M. He, *JHEP* **12**, 1 (2015).

[42] F.-K. Guo, U.-G. Meißner, W. Wang, Z. Yang, *Phys. Rev. D* **92**, 071502 (2015).

[43] Q. Wang, X.-H. Liu, Q. Zhao, *Phys. Rev. D* **92**, 034022 (2015).

[44] R.-Q. Wang, *et al.*, *Phys. Rev. C* **94**, 044913 (2016).

[45] G. Eichmann, H. Sanchis-Alepuz, R. Williams, R. Alkofer, C. S. Fischer, *Prog. Part. Nucl. Phys.* **91**, 1 (2016).

[46] C. D. Roberts, A. G. Williams, *Prog. Part. Nucl. Phys.* **33**, 477 (1994).

[47] M. Blank, A. Krassnigg, *Comp. Phys. Com.* **182**, 1391 (2011).

[48] A. Buck, R. Alkofer, H. Reinhardt, *Phys. Lett. B* **286**, 29 (1992).

[49] V. Mader, G. Eichmann, M. Blank, A. Krassnigg, *Phys. Rev. D* **84**, 034012 (2011).

[50] J. Nogueira, *et al.*, *Phys. Rev. D* **100**, 016021 (2019).

[51] W. Press, B. Flannery, S. Teukolsky, W. Vetterling, *Numerical Recipes in FORTRAN 77: Volume 1 of Fortran Numerical Recipes: The Art of Scientific Computing* (Cambridge University Press, 1992).

[52] G. Eichmann, *Few-Body Syst.* **58**, 81 (2017).

[53] S. Ahlig, R. Alkofer, *Annals Phys.* **275**, 113 (1999).

[54] Y.-R. Liu, H.-X. Chen, W. Chen, X. Liu, S.-L. Zhu **107**, 237 (2019).

[55] J. He, *Eur. Phys. Jour. C* **79**, 1 (2019).

[56] G. Eichmann, P. Duarte, M. Peña, A. Stadler, *Phys. Rev. D* **100** (2019).

[57] P. Zyla, *et al.*, *Prog. Theor. Exp. Phys.* **2020**, 083C01 (2020).

Appendix A

Numerical details

A.1 Momentum-partitioning

The Bethe-Salpeter equation can be solved by iteration within the range $P^2 \in \{M^2_{min}, M^2_{max}\}$ where M_{max} is determined from the singularity structure of the equation's through the baryon propagator, for instance.

Let p_+ and p_- be the baryon and meson momenta given, respectively, by:

$$p_+ = p + \eta P; \quad p_- = p - (1-\eta)P\,, \tag{A.1}$$

where, $\eta \in [0,1]$ is the momentum partitioning parameter.

The square of the onshell total momentum of the system is complex, and it is given by $\sqrt{P^2} = iM$, and thus also the p_+ and p_- are complex:

$$\begin{aligned} p_+^2 &= p^2 - \eta^2 M^2 + 2i\,\eta\, M\sqrt{p^2}\,\hat{p}\cdot\hat{P} \\ p_-^2 &= p^2 - (1-\eta)^2 M^2 + 2i\,(1-\eta)\, M\sqrt{p^2}\,\hat{p}\cdot\hat{P}\,, \end{aligned} \tag{A.2}$$

where $\hat{p}$ is the normalized momentum given by $\hat{p} = p/\sqrt{p^2}$.

These equations define the interior of a parabola $(p \pm i\eta M)^2$ or $(p \pm i(1-\eta)M)^2$, which is constrained by the nearest singularity in the particle X, which defines the limiting parabola at the mass pole m_X,

$$p_X^2 = (t \pm i m_X)^2, \tag{A.3}$$

where m_X represents the mass of the baryon, in our meson-baryon case.

This leads to the following restriction for the two-body case:

$$M < \min\left\{\frac{m_X}{\eta}, \frac{m_Y}{1-\eta}\right\}, \tag{A.4}$$

where m_Y is the mass of the meson.

Then, it is possible to find an optimal η value that allows calculations until the mass threshold, M.

In general, the momentum partitioning is arbitrary, and we could also distribute the momenta differently since the physics cannot depend on this parameter.

A.2 Four-momentum

The four-momenta are explicitly given by:

$$P^\mu = iM \begin{pmatrix} 0 \\ 0 \\ 0 \\ 1 \end{pmatrix}, \quad p^\mu = \sqrt{p^2} \begin{pmatrix} 0 \\ 0 \\ \sqrt{1-z^2} \\ z \end{pmatrix}, \quad q^\mu = \sqrt{q^2} \begin{pmatrix} 0 \\ \sqrt{1-z'^2}\sqrt{1-y^2} \\ \sqrt{1-z'^2}\, y \\ z' \end{pmatrix} \tag{A.5}$$

where, z, z' and y are the angular variables defined as:

$$z = \hat{p} \cdot \hat{P}, \quad z' = \hat{q} \cdot \hat{P}, \quad y = \hat{q}_\perp \cdot \hat{p}_\perp \quad , \tag{A.6}$$

where, the " $\hat{}$ " is the normalized four-vector (for instance, $\hat{p} = p/\sqrt{p^2}$), and the "$\perp$" represents the transverse part of the four-vector (e.g. $\hat{p}_\perp = \hat{p} - (\hat{p} \cdot \hat{P})\hat{P} = p - z\hat{P}$). For instance, the normalized and transverse p vector are explicitly written as:

$$\hat{p}^\mu = \begin{pmatrix} 0 \\ 0 \\ \sqrt{1-z^2} \\ z \end{pmatrix}, \quad p_\perp^\mu = \begin{pmatrix} 0 \\ 0 \\ \sqrt{1-z^2} \\ 0 \end{pmatrix} \tag{A.7}$$

A.3 Angular dependence and Chebyshev expansion

The kernel and propagator matrices given in eqs. (4.6) and (4.8), respectively, depend on the angular variables z and z' acquired from the the Euclidean scalar products of the involved momenta, given by:

$$z = \cos\theta = \hat{p} \cdot \hat{P} \quad and \quad z' = \cos\theta' = \hat{q} \cdot \hat{P} \tag{A.8}$$

where θ and θ' are the angles between the respective momenta, and $-1 < z, z' < 1$.

Therefore, one can expand any function $f(z)$ into Chebyshev polynomials $Y_m(z)$:

$$f(z) = \sum_{n=0}^{\infty} f_n\, Y_n(z)\,, \quad \text{and} \quad f_n = \int_{-1}^{1} dz\, \Omega_Y(z)\, Y_n^*(z)\, f(z)\,, \tag{A.9}$$

where $\Omega_Y(z)$ represents the integral measures and f_n are the coefficients of the expansion.

The Chebyshev polynomials satisfy the following orthogonality relation:

$$\int_{-1}^{1} dz\, \Omega_Y(z) Y_m^*(z)\, Y_n(z) = \delta_{mn}\,. \tag{A.10}$$

In our calculations, we use Chebyshev polynomials of the second kind $U_n(z)$. The expansion and respective coefficients are written as:

$$f(z) = \sum_n f_n \, U_n(z) \quad \text{and} \quad f_n = \frac{2}{\pi} \int_{-1}^{1} dz \, f(z) \, U_n(z) \sqrt{1 - z^2} \, , \tag{A.11}$$

where the integration weight is $\Omega_Y(z) = \frac{2}{\pi}\sqrt{1-z^2}$. The second kind Chebyshev polynomials are given by:

$$\begin{aligned} U_1 &= 1 & U_4 &= 16z^4 - 12z^2 + 1 \\ U_2 &= 2z & U_5 &= z\,(32z^4 - 32z^2 + 6) \\ U_3 &= z\,(8z^2 - 4) & U_6 &= 64z^6 - 80z^4 + 24z^2 - 1\,. \end{aligned}$$

In our calculations, we expand the angular dependence in z and z' only until order six.

Appendix B

Particle List

In the following table we present the mass, quark content, spin and parity of the particles considered in our calculations (see Figure 3.4). As previously announced, we assume isospin symmetry, so quarks u and d are denoted generally by q. The masses given in Table B.1 are approximated by the mass of the lightest particle with that quark content.

Particle	Quark content	Mass (GeV)	J^P
Σ_c	cqq	2.45	$\frac{1}{2}^+$
p	qqq	0.94	$\frac{1}{2}^+$
D	$c\overline{q}$	1.86	0^-
D^*	$c\overline{q}$	2.01	1^-
η_c	$c\overline{c}$	2.98	0^-
J/ψ	$c\overline{c}$	3.10	1^-
π	$q\overline{q}$	0.14	0^-
σ	$q\overline{q}$	0.45	0^+
ρ	$q\overline{q}$	0.77	1^-

Table B.1: List of the relevant properties of the particles used in this work, namely quark content, mass and J^P.

All these properties were taken from the most recent version of the Review of Particle Physics (August, 2020) [57].